Monthly Notices of the ROYAL ASTRONOMICAL SOCIETY

MNRAS **536,** 572–591 (2025) https://doi.org/10.1093/mnras/stae2601
Advance Access publication 2024 November 20

Miscentring of optical galaxy clusters based on Sunyaev–Zeldovich counterparts

Jupiter Ding ,[1,2]★ Roohi Dalal ,[1,3,4] Tomomi Sunayama,[5] Michael A. Strauss,[1] Masamune Oguri,[6,7] Nobuhiro Okabe ,[8] Matt Hilton ,[9,10] Rogério Monteiro-Oliveira,[11] Cristóbal Sifón [12] and Suzanne T. Staggs[13]

[1]*Department of Astrophysical Sciences, Princeton University, Peyton Hall, Princeton, NJ 08544, USA*
[2]*CIERA and Department of Physics and Astronomy, Northwestern University, 2145 Sheridan Road, Evanston, IL 60208, USA*
[3]*Department of Physics and Astronomy, University of British Columbia, Vancouver, BC V6T 1Z1, Canada*
[4]*Department of Political Science, University of British Columbia, Vancouver, BC V6T 1Z1, Canada*
[5]*Department of Astronomy and Steward Observatory, University of Arizona, Tucson, AZ 85721, USA*
[6]*Center for Frontier Science, Chiba University, 1-33 Yayoi-cho, Inage-ku, Chiba 263-8522, Japan*
[7]*Department of Physics, Graduate School of Science, Chiba University, 1-33 Yayoi-Cho, Inage-Ku, Chiba 263-8522, Japan*
[8]*Physics Program, Graduate School of Advanced Science and Engineering, Higashi Hiroshima Campus, Hiroshima University, Hiroshima 739-8526, Japan*
[9]*Wits Centre for Astrophysics, School of Physics, University of the Witwatersrand, Private Bag 3, 2050 Johannesburg, South Africa*
[10]*Astrophysics Research Centre, School of Mathematics, Statistics, and Computer Science, University of KwaZulu-Natal, Westville Campus, Durban 4041, South Africa*
[11]*Institute of Astronomy and Astrophysics, Academia Sinica, Taipei 10617, Taiwan*
[12]*Instituto de Física, Pontificia Universidad Católica de Valparaíso, Casilla 4059, Valparaíso, Chile*
[13]*Joseph Henry Laboratories of Physics, Jadwin Hall, Princeton University, Princeton, NJ 08544, USA*

Accepted 2024 November 18. Received 2024 November 14; in original form 2024 August 30

ABSTRACT

The ‘miscentring effect’, i.e. the offset between a galaxy cluster’s optically defined centre and the centre of its gravitational potential, is a significant systematic effect on brightest cluster galaxy (BCG) studies and cluster lensing analyses. We perform a cross-match between the optical cluster catalogue from the Hyper Suprime-Cam (HSC) Survey S19A Data Release and the Sunyaev–Zeldovich cluster catalogue from Data Release 5 of the Atacama Cosmology Telescope (ACT). We obtain a sample of 186 clusters in common in the redshift range $0.1 \le z \le 1.4$ over an area of 469 deg^2. By modelling the distribution of centring offsets in this fiducial sample, we find a miscentred fraction (corresponding to clusters offset by more than 330 kpc) of $\sim$25 per cent, a value consistent with previous miscentring studies. We examine the image of each miscentred cluster in our sample and identify one of several reasons to explain the miscentring. Some clusters show significant miscentring for astrophysical reasons, i.e. ongoing cluster mergers. Others are miscentred due to non-astrophysical, systematic effects in the HSC data or the cluster-finding algorithm. After removing all clusters with clear, non-astrophysical causes of miscentring from the sample, we find a considerably smaller miscentred fraction, $\sim$ 10 per cent. We show that the gravitational lensing signal within 1 Mpc of miscentred clusters is considerably smaller than that of well-centred clusters, and we suggest that the ACT SZ centres are a better estimate of the true cluster potential centroid.

Key words: gravitational lensing: weak – catalogues – galaxies: clusters: general – cosmological parameters.

1 INTRODUCTION

As the most massive gravitationally self-bound objects in the Universe, galaxy clusters are remarkably useful probes of both galaxy evolution and cosmology.The formation and evolution of brightest cluster galaxies (BCGs), the most luminous and massive galaxies in the Universe, are likely influenced by merger processes and other astrophysical phenomena within their host clusters (Hoessel & Schneider 1985; Postman & Lauer 1995; Lauer et al. 2014; Huang et al. 2018; Dalal et al. 2021). Moreover, clusters are strong probes of the growth of structure in the Universe, and they can be used to constrain cosmological parameters through abundance studies (Bahcall & Fan 1998; Allen, Evrard & Mantz 2011; Weinberg et al. 2013; Mantz et al. 2015; Garrel et al. 2022; Clerc & Finoguenov 2023). Measuring the galaxy weak lensing signal around a cluster (e.g. Rozo et al. 2010; Abbott et al. 2020; Sunayama et al. 2024) adds information about the halo mass to the abundance measurements, allowing one to simultaneously place strong constraints on both cluster masses and cosmology.

Methods for observing or identifying clusters are varied; here, we describe three. Each of these methods relies on a different observa-

★ E-mail: jupiterding2029@u.northwestern.edu

tional probe to determine the bottom of the cluster's gravitational potential well; in other words, its gravitational 'centre'. The first method we describe relies on the Sunyaev–Zeldovich (SZ) effect (Sunyaev & Zeldovich 1972): electrons in a cluster's hot intracluster medium (ICM) can scatter photons from the cosmic microwave background (CMB) to higher energies via inverse-Compton scattering. As a result, in CMB maps taken at frequencies below 220 GHz, clusters appear as 'cold' or darkened spots. Such a signal traces the cluster's gas – more precisely, the SZ signal at a specific position on the sky is proportional to the integrated gas pressure along the line of sight within the cluster. The cluster's SZ centre is then defined as the centroid of the SZ signal. Since the cluster's gas should generally trace the mass distribution, the SZ centre should coincide with the bottom of the cluster's potential well, especially when the cluster is fully virialized (Kravtsov & Borgani 2012).

A second method for identifying clusters relies on optical data. Optical surveys identify clusters by looking for closely concentrated collections of galaxies on the sky located at similar redshifts (e.g. Kim et al. 2002; Gladders & Yee 2005; Yang et al. 2007; Oguri 2014; Rykoff et al. 2014), as measured either photometrically or with a spectroscopic survey. Some cluster-finding algorithms define a cluster's optical centre as the location of the 'central galaxy;' i.e. a bright, massive galaxy located near the peak of the cluster's galaxy distribution. This is because the central galaxy often coincides with the bottom of its cluster's gravitational potential well as a result of dynamical friction (Chandrasekhar 1943): when a relatively massive galaxy moves within a cluster, it experiences a gravitational drag force from the surrounding matter, causing it to spiral in towards the gravitational centre (Ostriker & Tremaine 1975; Hausman & Ostriker 1978; Binney & Tremaine 2008).

However, there are situations where the central galaxy does not coincide with the gravitational centre. For example, consider two clusters in the process of merging. If they are close enough to each other, an optical cluster-finding algorithm may identify the system as one cluster even if it has not yet reached gravitational equilibrium; a typical relaxation time for a cluster merger is a few billion years (Faltenbacher, Gottloeber & Mathews 2006; Machado et al. 2015). Consequently, there may not yet be a bright, massive galaxy sufficiently close to the gas profile centre of the merged cluster. Alternatively, if the merging cluster is not yet fully virialized, there would not even be a well-defined bottom of the potential well. In both cases, one would be unable to accurately identify the cluster centre using a central galaxy.

Lastly, X-ray cluster surveys (e.g. Ebeling et al. 1998; Pacaud et al. 2007; Liu et al. 2022), similar to SZ cluster surveys, can trace the hot gas in a cluster: the ICM of a cluster emits X-rays via bremsstrahlung (or free–free) radiation.

Previous miscentring studies have generally shown that, around 20–40 per cent of the time, the central galaxy is *not* a good indicator of the bottom of a cluster's potential well (Sehgal et al. 2013; Lauer et al. 2014; Rykoff et al. 2016; Oguri et al. 2018; Hollowood et al. 2019; Zhang et al. 2019; Bleem et al. 2020; Yan et al. 2020). This number is referred to as the *miscentred fraction*.[1] In such studies, including this one, it is assumed that the cluster centre derived from a gas profile (i.e. from SZ or X-ray data) is a good indicator of the bottom of the potential well, while a cluster's optical centre may be displaced from the bottom of the potential well.

[1]We will also use the term *well-centered fraction*, which refers to the fraction of clusters for which the central galaxy *is* a good indicator of the gravitational centre.

Miscentring is a major systematic effect in cluster lensing analyses which constrain cosmological parameters with the cluster mass function (McClintock et al. 2019). Such studies take the lensing signals of optical clusters, model their azimuthally averaged mass profiles, and combine this with an inference of cluster abundance as a function of some optically based variable, e.g. richness. Richness is a measure of the number of galaxies in a cluster above some luminosity or mass threshold; we denote it in this paper as λ. (Note that the CAMIRA catalogue, discussed in Section 2.1.1, denotes richness with N_{mem}.) Miscentring of clusters impacts this measurement in several ways: first, the azimuthally averaged cluster lensing signal is suppressed because one is not centring the lensing signal on the true centre of the cluster's mass profile. Furthermore, miscentring leads to the underestimation of the number of clusters above a certain richness threshold (Zhang et al. 2019). Therefore, cluster lensing analyses explicitly account for the miscentred fraction in order to obtain estimates of cosmological parameters (e.g. Rozo et al. 2010; Abbott et al. 2020; Sunayama et al. 2024; Kelly et al. 2024). Additionally, BCG studies often define the BCG as the cluster's central galaxy (e.g. Oguri et al. 2018), so miscentring can introduce a bias in BCG samples. For example, Dalal et al. (2021) showed that BCGs with large displacements from the cluster centre tend to be less dominant than BCGs that are not. Finally, miscentring studies can point us towards interesting astrophysics within clusters (e.g. mergers) that contribute to miscentring (and may also influence BCG evolution).

In this paper, we aim to evaluate potential causes of the miscentring effect. As discussed previously, there may be astrophysical processes like mergers that cause central galaxies to be offset from the gas profile centre. We also explore non-astrophysical causes of miscentring, which include systematic effects in optical cluster data. Broadly speaking, our work illuminates potential directions for improvement in optical cluster-finding algorithms. In the context of BCG studies and cluster cosmology, we hope that identifying causes of miscentring will allow for more effective quantification and mitigation of this systematic effect.

This paper is structured as follows: in Section 2, we describe our cross-match between an optical cluster catalogue, drawn from the imaging data of the Hyper Suprime-Cam (HSC) survey, and an SZ cluster catalogue from the Atacama Cosmology Telescope (ACT) survey. The result is a matched sample that is larger and deeper than those used in many previous miscentring studies. In Section 3, we model the distribution of centring offsets within the fiducial sample and infer the fraction of clusters that are miscentred. In Section 4, we examine the optical image of each miscentred cluster and identify one of several potential causes of the miscentring. We then remove clusters with non-astrophysical causes of miscentring from our analysis and characterize the distribution of offsets among the remaining clusters. We summarize the results, potential implications, and avenues for future work in Section 6. Throughout our analysis, we assume a ΛCDM cosmology with $H_0 = 70$ km s^{-1} Mpc^{-1} or $h = 0.7$, $\Omega_{m,0} = 0.3$, and $\Omega_{\Lambda,0} = 0.7$.

2 DATA

2.1 Cluster catalogues used

In this study, we cross-match an optical cluster catalogue (Oguri et al. 2018) from the Hyper Suprime-Cam (HSC) Subaru Strategic Program (Aihara et al. 2018) with an SZ cluster catalogue from the Atacama Cosmology Telescope (ACT) (Hilton et al. 2021). In particular, we use the optical catalogue from the HSC S19A data release (Aihara et al. 2022) along with the SZ catalogue from Data

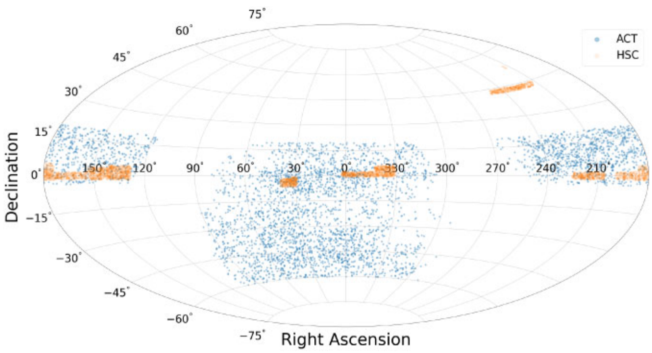

Figure 1. Sky map, in equatorial coordinates, of the positions of the clusters in the HSC and ACT catalogues used to create the fiducial sample. In total, we considered 5860 HSC clusters with $\lambda > 15$ and 4195 ACT clusters. The overlap in area between these two catalogues is 469 deg^2.

Release 5 of ACT (DR5; Naess et al. 2020); both catalogues are described in detail below. Fig. 1 shows the distribution on the sky of the clusters considered in the cross-match.

2.1.1 HSC catalogue

The Hyper Suprime-Cam is a wide-field optical imaging camera installed on the Subaru 8.2-m telescope (Miyazaki et al. 2018). The HSC survey (Aihara et al. 2018) has three layers – wide, deep, and ultradeep. In the completed survey, the HSC Wide layer, which we use in this work, has observed a sky area of $\sim 1200\ \mathrm{deg}^2$ with five broad-band filters (*grizy*; Kawanomoto et al. 2018). The HSC survey is unprecedented in that its depth ($i_{\mathrm{lim}} \sim 26$ at 5σ for point sources) is sufficient to construct a large sample of optically observed clusters up to $z \sim 1.4$ (Oguri et al. 2018). In this work, we use the HSC S19A wide-field, star-masked catalogue (the star masks used in the HSC survey are discussed in Section 4.2.) The S19A data release of the HSC survey consists of data taken between March 2014 and April 2019, covering an area of $\sim 589\ \mathrm{deg}^2$.

The cluster catalogue itself is created via the CAMIRA (Cluster-finding Algorithm based on Multiband Identification of Red-sequence gAlaxies) algorithm (Oguri 2014; Oguri et al. 2018). In short, CAMIRA searches for overdensities of red-sequence galaxies that are similar in both photometric redshift and position on the sky. CAMIRA identifies the cluster's centre as the position of a massive galaxy near the peak of the cluster's galaxy distribution; this is often, but not always, the *brightest cluster galaxy* (BCG), or the most luminous galaxy in the cluster. Additionally, CAMIRA uses stellar population synthesis models to compute a cluster's photometric redshift from the cluster's high-confidence member galaxies. The S19A CAMIRA catalogue consists of clusters in the redshift range $0.1 \leq z \leq 1.38$.

We emphasize that BCGs and central galaxies (as described in Section 1) are *not* always interchangeable terms. The definition of BCG varies between studies: for example, Lauer et al. (2014) and Dalal et al. (2021) use the literal definition of BCG (namely, the brightest galaxy in the cluster), while Oguri (2014) defines a BCG as the most luminous galaxy among galaxies close to the peak of the cluster's galaxy distribution. Hence, Oguri (2014) uses BCG and central galaxy interchangeably. For the sake of clarity, we follow Dalal et al. (2021) and avoid using the term 'BCG' when referring to the central galaxy.

One should also note that the task of identifying an optical cluster – including its member galaxies and centre – is not straightforward. In trying to identify a candidate central galaxy as a cluster's centre, one must have a general understanding of which galaxies belong to the cluster. However, in deciding which galaxies belong to a cluster, one must consider how close these galaxies are to the cluster centre. Therefore, identifying the optical centre is an inherently iterative process. In practice, CAMIRA uses a likelihood function to determine the most likely central galaxy for a given cluster candidate and then assigns a membership probability to each galaxy assigned to the cluster. This probability is based in part on its distance from the central galaxy, where the central galaxy has a membership probability of 1.

2.1.2 ACT catalogue

The SZ catalogue presented here comes from ACT Data Release 5; the catalogue is constructed from ACT observations obtained from 2008 to 2018 (Naess et al. 2020). The catalogue covers 13 211 deg^2 of the sky, with an overlap of 469 deg^2 with the HSC S19A wide survey. To search for clusters, Hilton et al. (2021) apply a multifrequency matched filter simultaneously to two sky maps from Naess et al. (2020) – one each at 90 and 150 GHz. The filter has a spatial component, which searches for cluster-sized objects, and a spectral component, which weights the signal according to the known spectral dependence of the SZ effect. Afterwards, Naess et al. (2020) compile a list of the SNR peaks; these are the cluster candidates (Hilton et al. 2023a). To create the final cluster catalogue, Hilton et al. (2021) match their candidates with optical imaging surveys, including the Sloan Digital Sky Survey (SDSS) (Ahumada et al. 2020), the Dark Energy Survey (DES) (Abbott et al. 2018), and HSC, in addition to estimating photometric redshifts by applying the `zCluster` algorithm (Hilton et al. 2023b) to photometric data from the Dark Energy Camera Legacy Survey (DECaLS; Dey et al. 2019), the Kilo Degree Survey (KiDS, Wright et al. 2019), and SDSS.

In this work, we perform an independent cross-match between the final list of ACT candidates and the HSC catalogue (see Section 2.2). This is because the ACT cluster data set (Hilton et al. 2021) does not include HSC cluster data for each ACT cluster with an HSC match; instead, some of these clusters are listed with optical data based on other surveys. We did not, however, cross-check the initial list of ACT cluster candidates with the HSC catalogue. For $\mathrm{SNR}_{2.4} \gtrsim 5.0$,[2] more than 95 per cent of ACT cluster candidates within the HSC footprint are optically confirmed (see fig. 15 in Hilton et al. 2021.) Therefore, an independent cross-match of the SNR peaks list with the HSC catalogueis unlikely to identify many new ACT candidates as clusters.

Unlike with optical data, SZ maps enable the identification of massive clusters at any redshift, as the strength of the SZ effect does not depend on the cluster's distance to the observer. For this reason, having a deep optical cluster catalogue – in this case, the HSC catalogue, which extends beyond $z \sim 1$ – allows us to construct a uniquely large cross-matched sample. One does not expect all ACT clusters in the HSC footprint to have a match in the HSC catalogue, because some ACT clusters may be at higher redshifts than those probed by HSC. (As mentioned in the previous paragraph, $\lesssim 5$ per cent of ACT cluster candidates lack an optical counterpart.) On the other hand, one does not expect all HSC clusters to have a match in the ACT catalogue: less massive HSC clusters are less

[2] As defined in Hilton et al. (2021), $\mathrm{SNR}_{2.4}$ is the SZ signal's signal-to-noise ratio at Hilton et al. (2021)'s reference 2.4 arcmin filter scale.

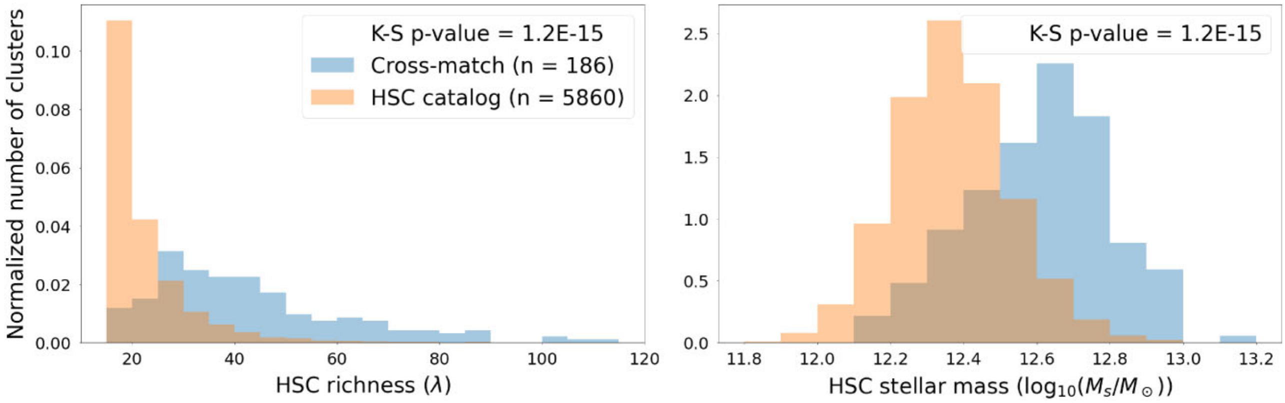

Figure 2. The normalized distributions of richness and stellar mass for both the fiducial cross-match and the full catalogues, along with the corresponding K-S test *p*-values. All *p*-values are statistically significant, indicating that the two catalogues are drawn from different underlying distributions. (We use SCIPY's K–S function, whose minimum output *p*-value is effectively 1.2×10^{-15}.).

likely to have high-pressure gas that gives rise to a measurable SZ signal.

2.2 Fiducial cross-match

In creating the cross-matched sample for this study, we identify the nearest HSC cluster for each ACT cluster. We do so via the ASTROPY package[3] (Robitaille et al. 2013; Price-Whelan et al. 2018; Astropy Collaboration 2022). For a given cross-match between an ACT and HSC cluster, we calculate the (projected) physical offset by using the CAMIRA photometric redshift for the HSC cluster. We then impose a maximum possible physical offset of 1 Mpc h^{-1} (i.e. a matching radius) for the pair to be considered a match. Because clusters are $\sim$ 1 Mpc in size, a pair of HSC and ACT clusters separated by this distance or more are almost certainly distinct.

We only consider HSC clusters whose listed richness λ is greater than 15. At very low richnesses, the HSC catalogue is both less complete and more contaminated with false clusters due to projection effects. Furthermore, as discussed in Section 2.1.2, the ACT catalogue is unlikely to contain low-mass/low-richness clusters, so cross-matches between an ACT signal and a low-richness HSC cluster would be suspect.

After imposing the matching radius, we remove cross-matches that include ACT clusters with an associated warning in the ACT catalogue. There are six such cases: one ACT cluster has a warning due to a potentially unreliable redshift; three clusters are associated with systems that may be two clusters at different redshifts projected onto each other; and the last two clusters were only confirmed via 'scanning mode', i.e. by running CAMIRA on an SZ position and identifying an optical cluster there that was not originally in the HSC catalogue. We remove these latter two clusters because their optical centres are dependent on ACT data.

Lastly, there is one case in which two ACT clusters are matched to the same HSC cluster. Here, we accept the lower redshift ACT cluster as the true match. The resulting sample contains 186 clusters with redshifts between 0.1 and 1.4 within an area of 469 deg^2; this is the largest existing cross-matched sample that uses HSC data. Throughout this paper, we refer to this sample as the fiducial cross-match or the fiducial sample.

[3]Specifically, we use the method `match_to_catalog_sky` from the `SkyCoord` class.

In addition to the fiducial sample, we create a cross-match where the matching radius is a function of ACT SNR. We do this using the `nemo` algorithm (Hilton et al. 2023a), which also includes a conservative estimate for positional uncertainties in the optical catalogues by adding in quadrature an additional 0.5 Mpc projected distance to the cross-matching radius. This `nemo`-based sample excludes five clusters contained in the fiducial sample, but is otherwise identical. These five excluded clusters are all highly miscentred; thus, one should suspect that systematic effects in the cross-matching and/or the CAMIRA algorithm may be relevant to these five cases. Indeed, in our analysis described in Section 4, we find that three of the excluded clusters are miscentred due to a star mask, one is miscentred due to an observational artefact, and one is miscentred due to a false ACT signal.

2.2.1 *Fiducial cross-match properties*

In Fig. 2, we plot the distributions of richness λ and stellar mass M_s for both the fiducial cross-match and the full catalogue. We use the values listed in the HSC catalogue. In brief, HSC defines richness as the sum of the membership probabilities of all galaxies in a cluster, and stellar mass is defined as the weighted sum of the individual galaxy masses, each of which are calculated using a stellar population synthesis model (Oguri 2014). In our richness distributions, the number of clusters generally decreases with richness, consistent with similar studies that use different optical and SZ catalogues (e.g. Grandis et al. 2021).

For both properties, we perform a two-sided Kolmogorov–Smirnov (K–S) test, which estimates the probability that two samples come from the same underlying continuous distribution; in the context of this work, we test if our cross-matched sample is representative of the underlying catalogues. As shown in Fig. 2, the *p*-value for each property is statistically significant, suggesting that the fiducial cross-match and the full catalogue have different underlying distributions. In particular, one sees that cross-match clusters are generally richer and have higher stellar mass. These trends are expected because, as Fig. 3 shows, richer/more massive clusters generally have stronger SZ signals; thus, lower richness/lower mass HSC clusters are less likely to have a match in the ACT catalogue.

Fig. 3 shows the completeness of the cross-matched sample as a function of HSC richness. This completeness is defined as the fraction of HSC clusters within a given richness bin that have a counterpart in the ACT catalogue. Consistent with similar cross-matching studies

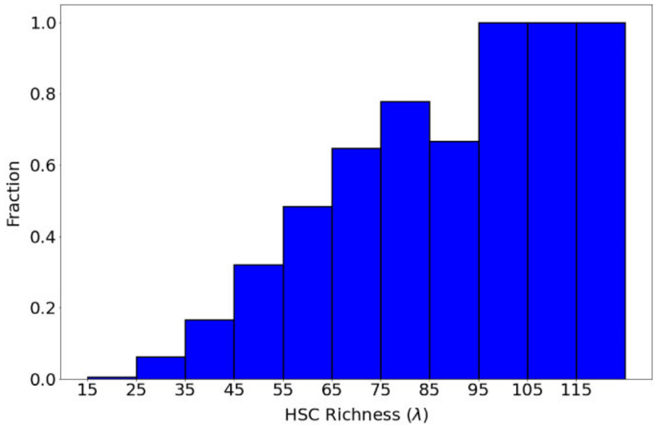

Figure 3. ACT completeness as a function of HSC richness. Completeness generally increases with richness, reaching 100 per cent for clusters with $\lambda \gtrsim 100$.

(e.g. Grandis et al. 2021), the completeness increases with richness, reaching 1 for the five clusters with $\lambda \gtrsim 100$.

The full sample of matched clusters, together with their offsets and our interpretations of them, are given in Appendix A.

3 CENTRING OFFSET MODEL

3.1 Offset distribution and model

We aim to construct a model of the distribution of centring offsets r within our fiducial cross-match. Here, r is the projected physical separation at the redshift of the cluster. In doing so, our goal is to infer the fraction of clusters that have an offset due to measurement uncertainty and the fraction that are miscentred due to other effects, such as mergers of clusters.

The histogram in Fig. 4 shows the normalized distribution of r for our fiducial cross-match. We model this distribution using the two-component model from Oguri et al. (2018):

$$p(r) = f_{\rm cen}\frac{r}{\sigma_1^2}\exp\left(-\frac{r^2}{2\sigma_1^2}\right) + (1 - f_{\rm cen})\frac{r}{\sigma_2^2}\exp\left(-\frac{r^2}{2\sigma_2^2}\right) \quad (1)$$

The first component models the well-centred cluster population, while the second component models the miscentred population; each individual component is modeled with a Rayleigh distribution, which assumes that the horizontal and vertical displacements on the sky are each normally distributed. Here, r is the offset in Mpc, $f_{\rm cen}$ is the fraction of clusters that are well-centred, and σ_1 and σ_2 are the characteristic offsets for the well-centred and miscentred populations, respectively.

We expect the positional error to be dominated by the SZ positional uncertainty: while optical astrometric errors on individual galaxies are less than 1 arcsec, the SZ positional uncertainty is on the order of $\gtrsim 10$ arcsec due to the resolution of the CMB maps. Given a typical value of $\mathrm{SNR}_{2.4} = 5$ for the fiducial sample, we expect a positional error of ~ 17 arcsec (see Hilton et al. 2021, who run the nemo algorithm on simulated ACT data and model the distribution of SZ positional uncertainty as a function of $\mathrm{SNR}_{2.4}$). This angle corresponds to a projected offset of ~ 0.15 Mpc over most of the redshift range of the catalogue. We thus fix $\sigma_1 = 0.15$ Mpc, and fit for $f_{\rm cen}$ and σ_2 simultaneously with a maximum-likelihood method.

Fig. 4 shows the measured and best-fitting offset distribution of the fiducial cross-match. The best-fitting parameters are $f_{\rm cen} = 0.75$ and $\sigma_2 = 0.39$ Mpc. This $f_{\rm cen}$ is consistent with previous miscentring studies, while σ_2 is consistent with Oguri et al. (2018), which reports $\sigma_2 = 0.26 \pm 0.04\,h^{-1}$ Mpc, approximately $\sigma_2 \sim 0.37$ Mpc for $h = 0.7$.

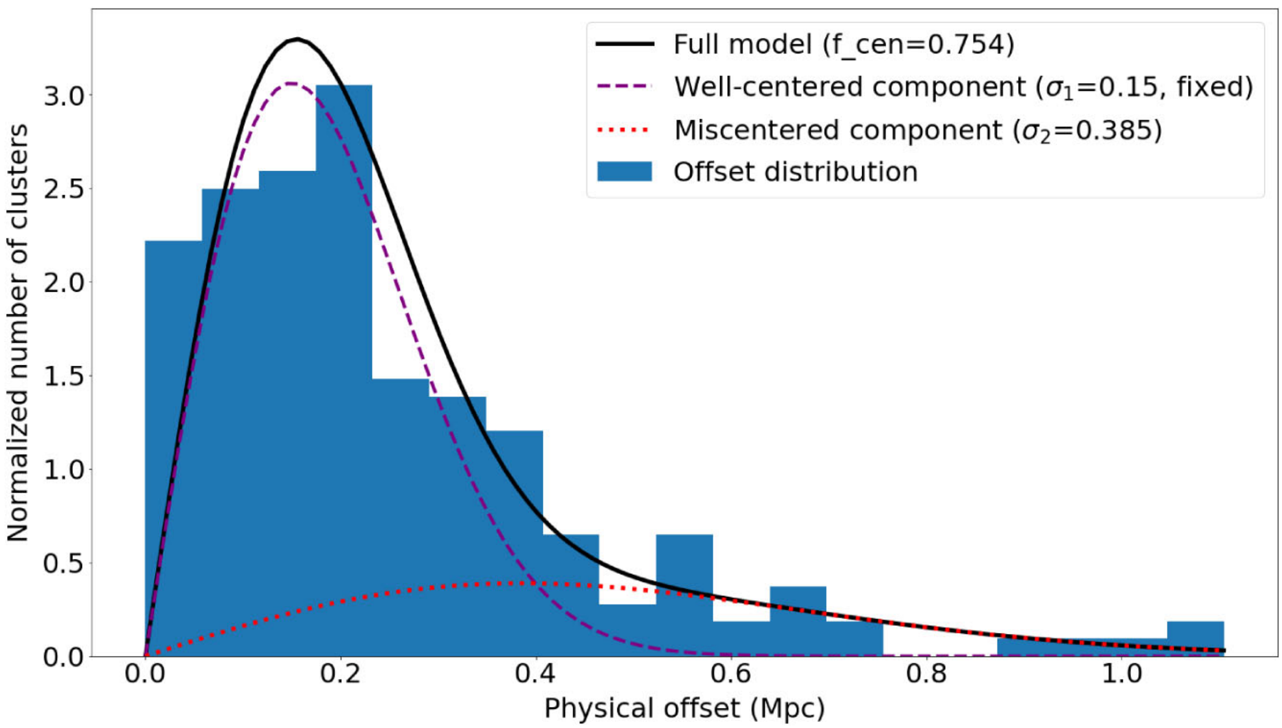

Figure 4. Offset distribution for the fiducial cross-match, including the histogram of measured offsets, the best-fit model using equation (1), and the two components of the model.

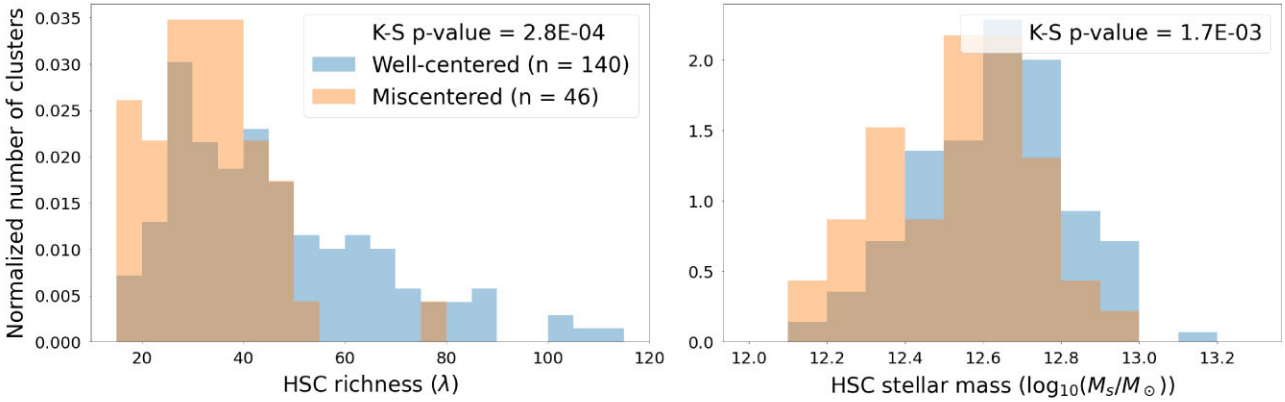

Figure 5. The normalized distributions of richness and stellar mass for both well-centred and miscentred clusters within the fiducial cross-match, along with the corresponding K–S test *p*-values. The *p*-values for λ and M_s are both statistically significant, indicating that miscentred clusters have lower richness and stellar mass than well-centred clusters.

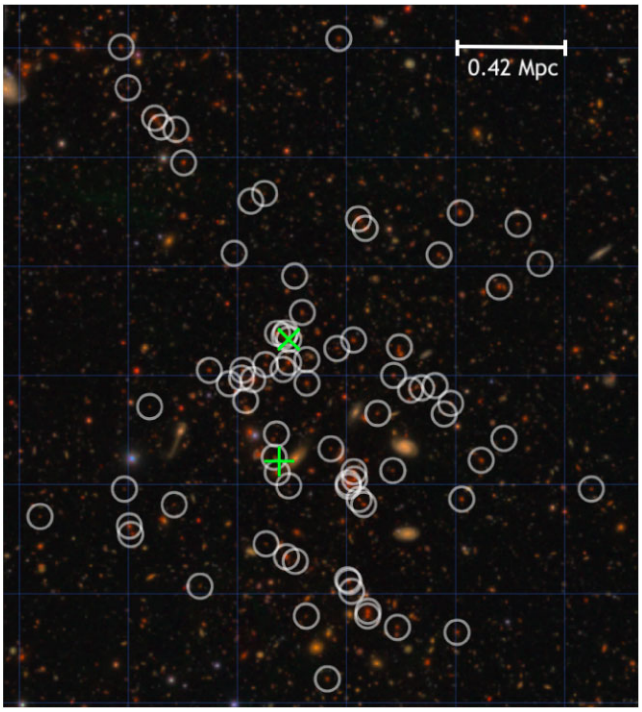

Figure 6. HSC cluster HSCJ142103+002322 at redshift $z = 0.65$, an example of a miscentred cluster that can be attributed to a merger. It has an offset of 0.47 Mpc. The + symbol indicates the ACT centre, the × symbol indicates the HSC centre, and the circles indicate member galaxies of the cluster with membership probability > 0.1 (we use this convention in subsequent figures as well). In this and subsequent figures, North is up and East is to the right; note that this differs from the usual convention of having East be to the left. The scale is shown with the scale bar in the figure. There appear to be three potential peaks in the cluster's galaxy distribution: one at the HSC centre, one to the right of the ACT centre, and one near the bottom of the image.

3.2 Well-centred versus miscentred populations

Based on our best-fitting model, $f_{\rm cen} = 0.754$ of the clusters in the fiducial cross-match are well-centred; these clusters have offsets of $r < 330$ kpc. Thus, we denote this value, 330 kpc, as the *well-centred cutoff*. The remainder of the clusters are labelled as miscentred. We acknowledge that this definition of the well-centred cutoff is somewhat arbitrary. In Section 5, we show that the difference in lensing signals between the well-centred and miscentred populations is statistically significant, thus validating our choice of the well-centred cutoff.

Following Fig. 2, Fig. 5 compares the distributions of λ and M_s between the well-centred and miscentred clusters. Here, the *p*-values of the K–S test for λ and M_s are statistically significant, suggesting that well-centred and miscentred clusters are not drawn from the same underlying distribution. Miscentred clusters generally have lower λ and M_s than do well-centred clusters. This may partially be explained by the fact that the inferred richness and mass of miscentred clusters are biased low by miscentring.

4 CAUSES OF MISCENTRING

In this section, we discuss potential causes of miscentring in the fiducial sample. Using the HSC S19A wide-field data release (Aihara et al. 2022), we individually examine the optical images of all 46 miscentred clusters in the fiducial sample. The cluster images shown in this paper (e.g. Fig. 6) are composites of images taken in the g, r, and i filters.

We find that causes of miscentring broadly fall into three categories: cluster mergers, systematic effects in the HSC data, and other causes such as potential false matches and false ACT signals. We also discuss miscentred clusters that seemingly lack any cause of miscentring. Table 1 summarizes the eight causes of miscentring discussed in our analysis, while Table A1 has the full list of clusters in our cross-match, including miscentring causes as relevant.

4.1 Merging clusters

As discussed in Section 1, cluster mergers are a potential astrophysical explanation for clusters with a large offset between the optical and SZ-defined centres. In merging systems, the gravitational potential may well not have a well-defined centre. Even if this centre is well-defined, then there might not be a bright, massive galaxy that has moved close enough to that centre yet. To determine which of our miscentred clusters are due to ongoing mergers, we compare our fiducial cross-match with a pre-existing catalogue of merging clusters in the HSC catalogue. This merger catalogue was created by looking for clusters with multiple peaks in their projected galaxy distributions (Okabe et al. 2019).

Table 1. A summary of the causes of miscentring identified in our analysis along with the number of miscentred clusters corresponding to each cause. We indicate the section of the text where each cause is described. The 'multiple possible causes' category indicates clusters that may be affected by multiple different causes of miscentring, and the 'no apparent cause' category indicates clusters without any apparent cause of miscentring.

Cause of miscentring	Number of clusters
Merger (Section 4.1)	14
Star mask (Section 4.2.1)	11
Observational artefact (Section 4.2.2)	2
Deblending (Section 4.2.3)	2
Misidentified central galaxy (Section 4.2.4)	2
False match (Section 4.3.1)	2
False ACT signal (Section 4.3.2)	3
Multiple possible causes (Section 4.3.3)	6
No apparent cause (Section 4.3.4)	4

Table 2. Merging statistics for the fiducial cross-match, based on a catalogue of optically identified merging clusters in the HSC catalogue (Okabe et al. 2019).

	Merging	Not merging	Total	Merging fraction
Well-centred	68	72	140	49 per cent
Miscentred	23	23	46	50 per cent
Total	91	95	186	49 per cent

Table 2 shows the results of the comparison, which indicates that 50 per cent of the miscentred clusters are undergoing mergers. We emphasize, however, that not all clusters identified as merging by Okabe et al. (2019) are miscentred solely due to an ongoing merger. For example, a cluster identified as a merger by Okabe et al. (2019) could also be miscentred due to a star mask over the true central galaxy (see Section 4.2.1). Therefore, the number of merging, miscentred clusters as listed in Table 2 exceeds the number of merging, miscentred clusters we identify in our sample (see Table 1).

The fraction of miscentred clusters which are merging is similar to that for well-centred clusters, indicating that mergers are *not* strongly correlated with miscentring. Furthermore, a non-negligible fraction of miscentred clusters are not mergers. It is possible that the merger catalogue in Okabe et al. (2019) is incomplete (i.e. missing some merger systems) or that there are other, not necessarily astrophysical processes that also contribute to miscentring. Investigating the former is outside the scope of this paper, as it would require an independent probe of cluster mergers; however, we explore the latter possibility in detail in Section 4.2.

In Fig. 6, we show an example of a cluster that we determine to be miscentred due an ongoing merger. In agreement with Okabe et al. (2019), we identify this cluster as a merger because there appears to be three potential peaks in this cluster's galaxy distribution. Additionally, the ACT centre is located between these peaks, further suggesting that this system consists of merging clusters.

In Appendix B, we compare the properties of merging and non-merging clusters within the cross-match.

4.2 Systematic effects in HSC data

Within the category of systematic HSC effects, we identify four causes of miscentring: masks due to bright stars, observational artefacts, galaxy deblending issues, and CAMIRA misidentification of the cluster's central galaxy. In total, 17 miscentred clusters fall into this category.

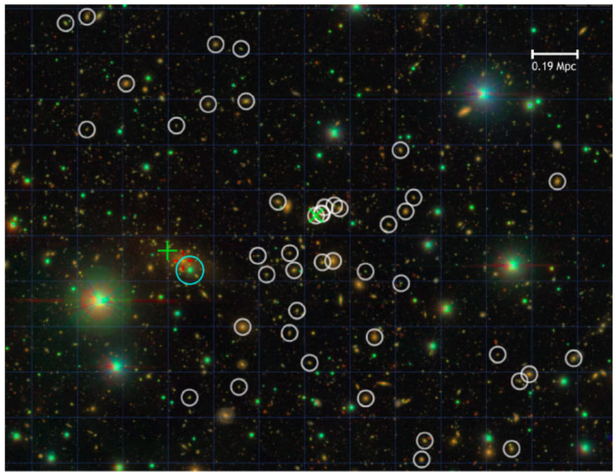

Figure 7. HSC cluster HSCJ090119+030156 at $z = 0.19$, an example of a miscentred cluster that can be attributed to the obscuring effects of a bright star with $G_{\rm Gaia} \sim 14.7$; this star is named Gaia DR3 578 211 316 549 315 584 (Gaia Collaboration 2022). The cluster has an offset of 0.65 Mpc. The cross-hairs (near the ACT centre) indicate the alternative central galaxy that is obscured by the star's circular mask, represented by the nearby larger circle. The offset using this alternative central galaxy is only 0.08 Mpc.

4.2.1 *Star masks*

Like all optical imaging surveys, HSC is affected by bright stars, whose extended point spread function can affect the detection and photometry of galaxies in their vicinity. For this reason, the galaxy sample on which the CAMIRA cluster catalogue is based has been trimmed of objects falling too close to bright stars (Coupon et al. 2018). However, if the resulting star mask overlaps the footprint of a cluster, the determination of its centre is likely to be biased or completely incorrect.

We find 11 clusters that are most likely miscentred due to the star mask within the HSC data. In these cases, we identify a potential alternative central galaxy at the same photometric redshift as the cluster, with high luminosity and an extended envelope. These alternative central galaxies were not identified by CAMIRA since they are either fully or partially covered by an HSC star mask; instead, CAMIRA has chosen a different central galaxy, one that is not representative of the cluster centre.

We determine if a star mask is obscuring an alternative central galaxy by calculating the extent of its star mask. Coupon et al. (2018) describe the procedure for building the HSC star masks: a major component for each mask is a circular mask with radius depending on the star's G-band magnitude in the *Gaia* catalogue (Gaia Collaboration 2023):

$$r[\text{arcsec}] = \begin{cases} 708.9 \times \exp(-G_{\rm Gaia}/8.41), & G_{\rm Gaia} < 9 \\ 694.7 \times \exp(-G_{\rm Gaia}/4.04), & G_{\rm Gaia} \geq 9. \end{cases} \quad (2)$$

In Fig. 7, we show an example of such a cluster, with an apparent offset of 0.65 Mpc. The large elliptical galaxy with an extended envelope near the ACT centre has a spectroscopic redshift of 0.19 (Ahn et al. 2012), the same as the cluster's photometric redshift, yet it is excluded from the cluster's member list. Furthermore, the offset between the ACT centre and the alternative central galaxy

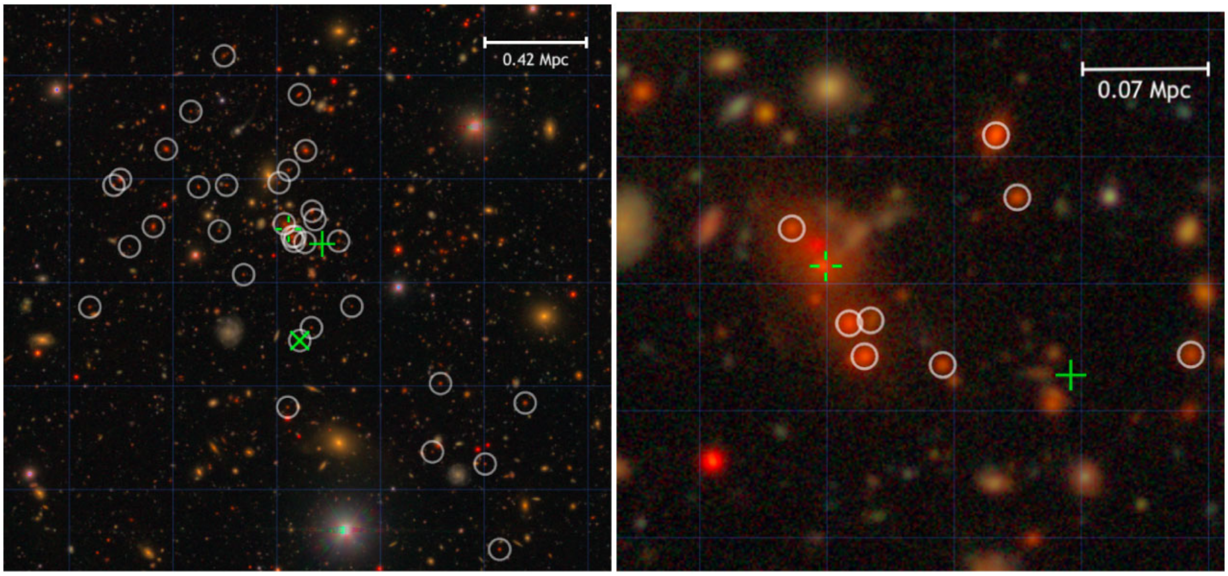

Figure 8. Left: HSC cluster HSCJ021002-024411 at $z \approx 0.66$, an example of a miscentred cluster that can be attributed to HSC image deblending issues. It has offset 0.40 Mpc. The cross-hairs indicate a potential alternative galaxy. Right: A close-up view of the same cluster near the ACT centre. Many of the overlapping galaxies near the ACT centre are not identified as individual sources in the HSC object catalogue, suggesting that they are not properly deblended. It is unclear if the marked object is a single galaxy, two galaxies in the process of merging, or two physically distinct galaxies; further, it is unclear whether one of these galaxies could be the true central galaxy of the cluster.

is only 0.08 Mpc. The exclusion of this galaxy from the CAMIRA member galaxy list is a result of the mask around the bright star with radius 18 arcsec. Because of this excluded galaxy, we believe that the CAMIRA-determined centre is likely incorrect, causing this cluster to be labelled as miscentred.

4.2.2 *Observational artefacts*

Similar to the star mask case, observational artefacts can contaminate images of HSC clusters, preventing CAMIRA from detecting the true central galaxy of a cluster. We find two such cases where an observational artefact either impacts the imaging of the entire cluster or passes through a likely central galaxy, resulting in that central galaxy not being identified by CAMIRA. Both of these cases appear to be the result of improper stacking of single-exposure images, resulting in bright streaks on the co-added image.

4.2.3 *Deblending issues*

In the crowded environments of galaxy clusters, the images of galaxies often overlap and need to be deblended to measure the brightness of each galaxy separately. The deblending algorithm, described in Bosch et al. (2018), occasionally fails, giving incorrect photometry of the individual galaxies. We found two such cases among our sample of miscentred clusters.

These deblending failures are identifiable by the fact that not every visible galaxy or component of a blend was identified in the HSC object catalogue. If deblending fails, then the true central galaxy may have an incorrect reported brightness or not be detected at all, among other potential issues. In either case, CAMIRA would select another galaxy as the centre, leading the cluster to be labelled as miscentred. We find two such miscentred clusters, one of which is shown in Fig. 8.

4.2.4 *Central galaxy misidentification*

For two miscentred clusters, we determine that the potentially true central galaxy was detected by CAMIRA and labelled as a member of the cluster – however, CAMIRA still chose a different galaxy as the centre. In particular, we see a large, elliptical galaxy in the cluster that is not chosen as the centre despite being both brighter and closer to the ACT centre than the CAMIRA-chosen centre. For both clusters, if the alternative central galaxy were selected instead, then the cluster's offset would fall below the well-centred cutoff of 330 kpc (Section 3.2).

4.3 Other causes

We identify two causes of miscentring that do not fall in the category of either mergers or systematic HSC effects: false matches between ACT and HSC clusters, and false ACT signals. We also identify two other subcategories: clusters that could be miscentred due to multiple potential factors, and clusters that lack any apparent cause of miscentring. In total, 15 miscentred clusters fall into the category of other causes.

4.3.1 *False match*

We suspect that two of the miscentred clusters arise from a false match between HSC and ACT clusters; i.e. when the corresponding ACT cluster is more likely to correspond to a different optical cluster that is not detected by CAMIRA. In both cases, the HSC cluster in the fiducial cross-match has a low richness (< 17). As discussed in Section 2.2, low-richness clusters tend to have weak SZ signals and are often undetected by ACT, making the match less convincing, and strengthening our conclusion that these clusters are miscentred due to false matches.

One example cluster is shown in Fig. 9. The ACT centre is $\sim$ 21 arcsec away from an overdensity of galaxies at $z \sim 0.6$, which we

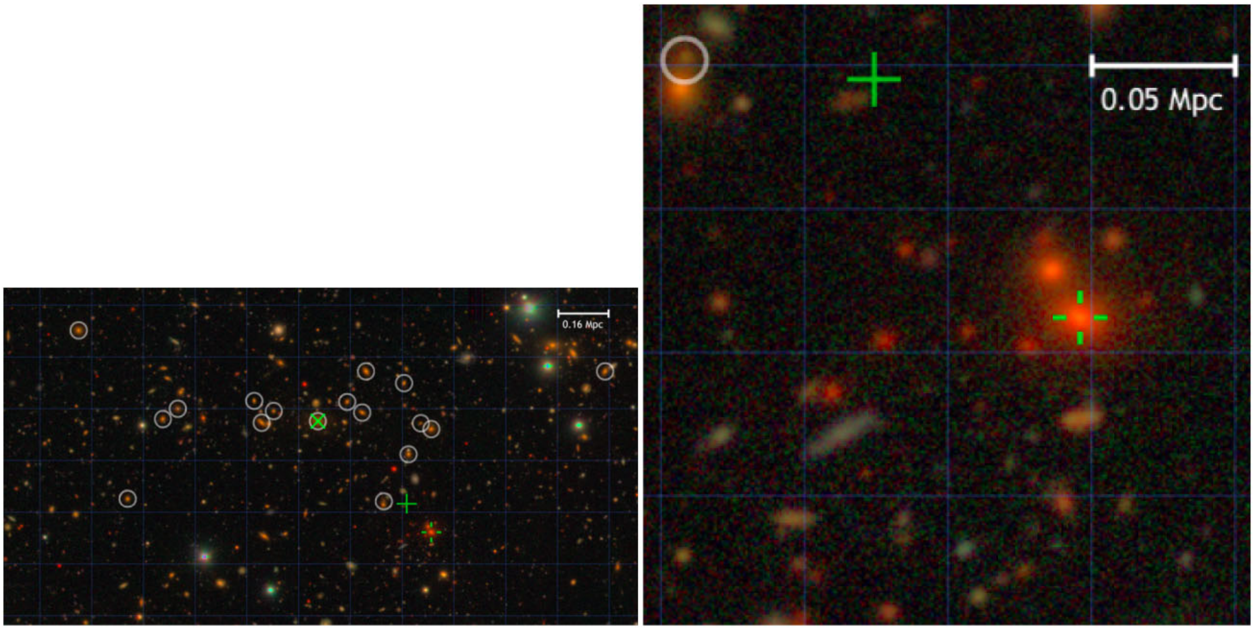

Figure 9. Left: HSC cluster HSCJ114409+044133 at $z \approx 0.41$, an example of a miscentred cluster that can be attributed to a false match between this cluster and an ACT cluster. It has offset 0.38 Mpc. We suspect that a galaxy overdensity near the ACT signal is an optical cluster missed by CAMIRA; its possible centre is indicated with the cross-hairs. If this cluster were the true source of the detected SZ signal, then its offset would only be 0.14 Mpc. Right: A close-up view of HSC cluster HSCJ114409+044133 near the centre of the potential second cluster.

suspect is an optical cluster unidentified by CAMIRA. If this is the true optical cluster corresponding to the ACT centre, then the offset would only be ~ 0.14 Mpc, which would change the cluster from miscentred to well-centred.

4.3.2 False ACT signal

Based on fig. 6 in Hilton et al. (2021), one should expect around 2000 false ACT signals – i.e. a signal not originating from a real cluster – within the full ACT DR5 map. These false signals are due to noise fluctuations in the CMB maps. It would be reasonable to assume that our cross-match contains at least a few spurious matches between a false ACT signal and an HSC cluster. Additionally, since matches between false signals and HSC clusters are essentially random, it is reasonable to expect occasional matches with large offsets that nevertheless fall within our matching radius of 1 Mpc h^{-1}. Assuming these signals are randomly distributed, then we expect ~ 70 false signals in the HSC footprint and estimate that ~ 13 of them would be cross-matched with an HSC cluster given that our matching circles cover ~20 per cent of the ACT-HSC overlap region. As mentioned in Section 2.1.2, Hilton et al. (2021) finds that more than 95 per cent of ACT cluster candidates within the HSC footprint are optically confirmed. However, given our calculation, it is feasible that at least a few of the real optical clusters (especially low-richness ones) were matched to false ACT signals.

In our sample, we find three miscentred clusters that appear to correspond to false signals in the ACT catalogue. For each cluster, we did not observe any apparent galaxy overdensity near the ACT centre. We confirmed this by looking at the SZ signal's contours (as explained in fig. 10 in Hilton et al. 2021), which had little to no overlap with the HSC cluster galaxy distribution. One such cluster is shown in Fig. 10. Because the ACT signal in the figure does not appear to correspond to any real cluster, we conclude that it is a false signal.

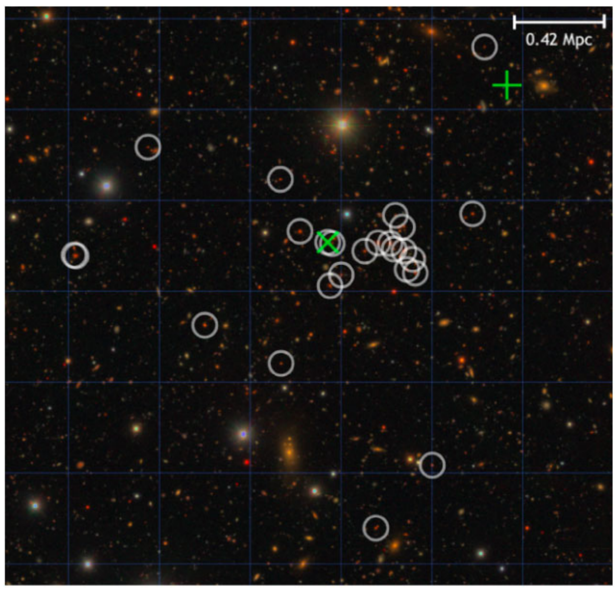

Figure 10. HSC cluster HSCJ135746+002431 at $z \approx 0.67$, an example of a miscentred cluster that can be attributed to this cluster being matched with a false ACT signal. There is no apparent galaxy overdensity near the ACT centre. The cluster has offset 1.1047 Mpc.

4.3.3 Multiple possible causes

We identify six miscentred clusters that each appear to show symptoms of several causes of miscentring, no one of which was clearly the sole reason for the miscentring. Fig. 11 shows one such cluster. It is unclear if the nearby, foreground galaxy is obscuring any cluster galaxies that would otherwise be detected by CAMIRA. For example, the true central galaxy might be obscured yet close to the ACT centre, which would mean that this cluster is actually well-

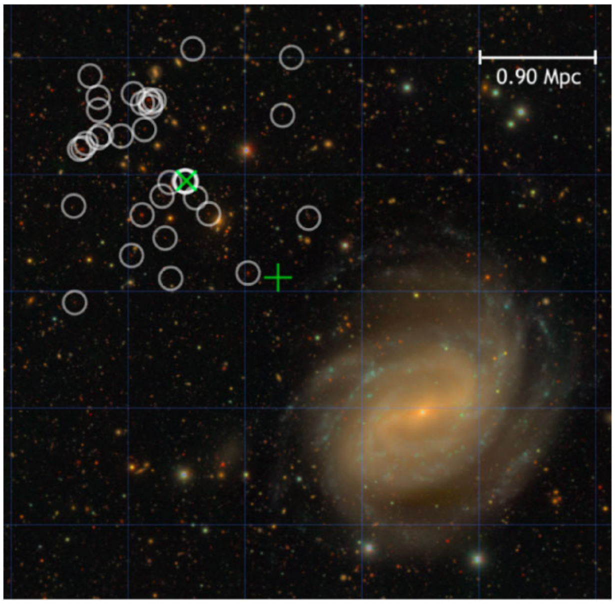

Figure 11. HSC cluster HSCJ120827+025640 at $z \approx 0.79$, an example of a cluster with multiple possible causes of miscentring: the obscuring foreground galaxy (NGC 4123), a merger, and/or a false ACT signal. It has offset 1.02 Mpc.

centred. It is also possible that the cluster is undergoing a merger but the foreground galaxy is obscuring one half of the merging cluster – thus, we only see the ACT signal located between the two halves of the merger. On the other hand, it may be true that the foreground galaxy does not obscure any cluster galaxies. In this case, the ACT signal might be a false signal that aligned with this HSC cluster by chance. The cluster has a relatively low richness of ∼ 20, meaning that it is unlikely to have a detectable ACT signal (although the obscuration of the bright galaxy could be causing CAMIRA to underestimate the richness).

4.3.4 *No apparent cause of miscentring*

We identify four clusters that lack any apparent cause of miscentring. In contrast with the false signal clusters, these clusters each have an ACT signal near a galaxy overdensity. Therefore, in each case, we believe that the offset is astrophysically real despite there being no evidence for an ongoing merger. In fact, when we refit the offset distribution with a 'cleaned' cluster sample (Section 4.4), the subsequent model yields a higher well-centred cutoff – as a result, the model labels three out of four of the 'no apparent cause' clusters as well-centred instead of miscentred.

4.4 Cleaned offset distribution

We create a 'cleaned' cluster sample by taking the fiducial sample and excluding all miscentred clusters that have a clear, non-astrophysical cause of miscentring; i.e. the clusters that are miscentred due to a systematic HSC effect (Section 4.2), a false match (Section 4.3.1), or a false ACT signal (Section 4.3.2). The resulting cleaned sample has 164 clusters. Fig. 12 shows the offset distribution of this cleaned sample, together with the best-fitting model (equation 1). Here, we find $f_{\rm cen} = 0.91$ and $\sigma_2 = 0.39$ Mpc.

This cleaned sample is separated into well-centred and miscentred populations using the same method described in Section 3.2; i.e. the cutoff is chosen such that $f_{\rm cen} = 0.91$ of the clusters are below the cutoff, and these clusters are labelled as well-centred. The cleaned sample's well-centred cutoff is 370 kpc, slightly larger than the fiducial sample's well-centred cutoff of 330 kpc. We find nine clusters

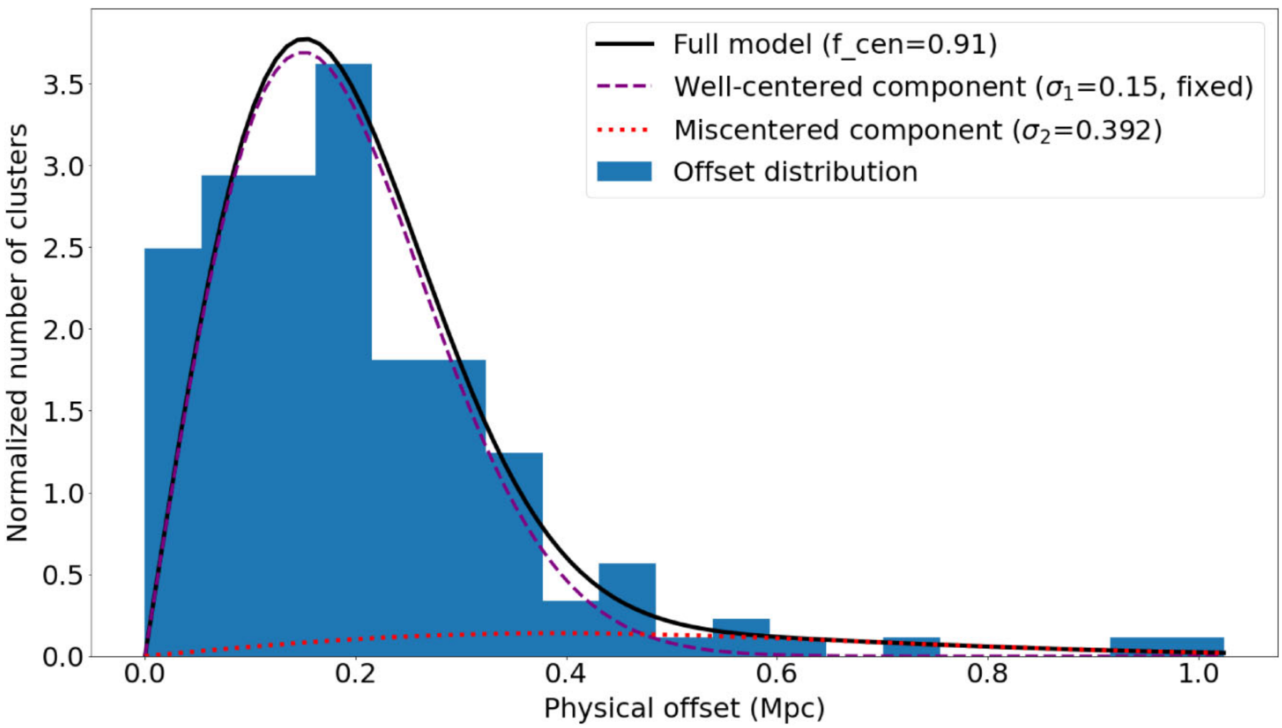

Figure 12. Offset distribution for the cleaned cross-match. The figure shows the offset histogram, the best-fitting model using equation (1), and the two components of the model, namely the well-centred and miscentred clusters.

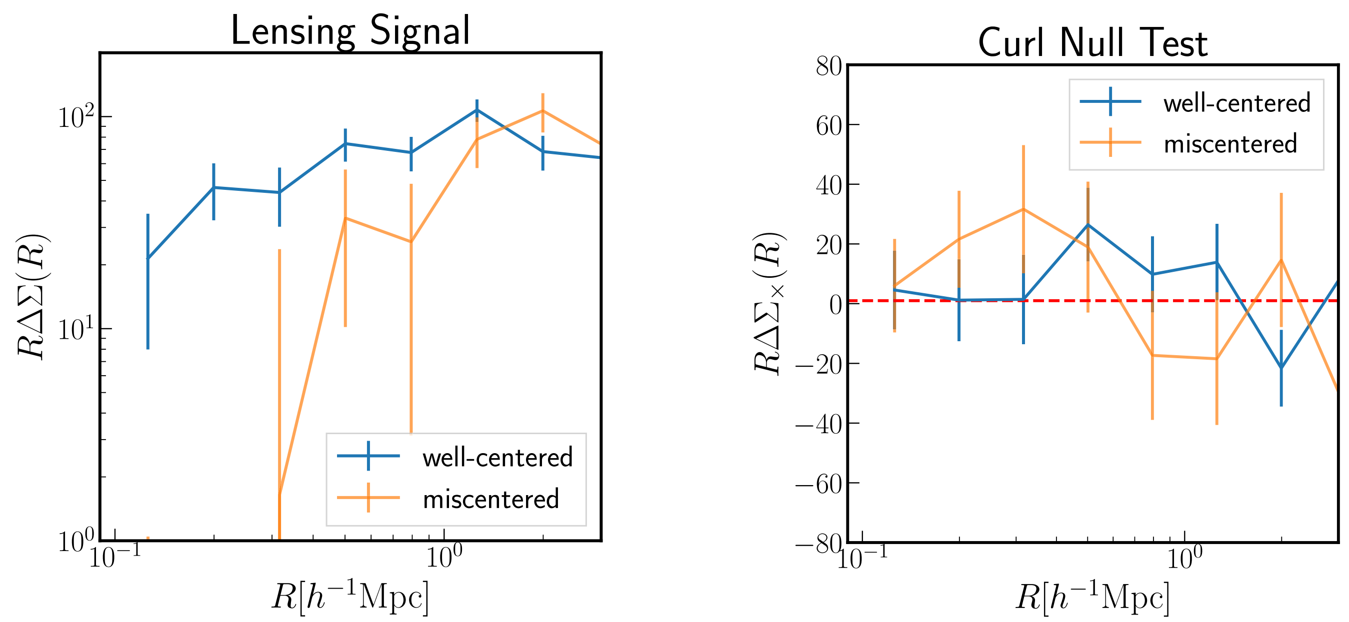

Figure 13. A comparison of the lensing signals for well-centred and miscentred clusters in the redshift range $0.3 < z < 0.7$. Here, we use the CAMIRA central galaxy as the cluster centre. $\Delta\Sigma(R)$ is the cluster's lensing signal as a function of radius, and $\Delta\Sigma_\times(R)$ is the lensing signal in the 45-degree rotated component. The error bars represent the intrinsic shape noise. Note that $\Delta\Sigma$ is multiplied by R to reduce the dynamic range in these plots. For the miscentred population, $\Delta\Sigma(R)$ is suppressed at small scales, as expected for miscentred clusters. $\Delta\Sigma(R)$ at the lowest radius is not shown for the miscentred clusters because it is negative with a large error bar. The difference in $\Delta\Sigma(R)$ between the well-centred and miscentred clusters is highly statistically significant, with a p-value of 6.6×10^{-6}.

within the cleaned sample that are miscentred in the fiducial sample but are well-centred in the cleaned sample; i.e. they each have an offset between 330 and 370 kpc. Six of these clusters were previously identified as being miscentred due to an ongoing merger, whereas the other three are 'no apparent cause' clusters. (There are four 'no apparent cause' clusters in total; the fourth, HSCJ231255-001521, has offset 535 kpc.) The fact that only one out of fifteen miscentred clusters in the cleaned sample is labelled as 'no apparent cause' affirms that our offset model accurately separates our clusters into well-centred and miscentred populations.

5 LENSING MEASUREMENTS

To understand the physical nature of the clusters we have identified as miscentred, we compare the weak gravitational lensing signals measured for the two sets of clusters using the Year 3 shape catalogue of the HSC survey (Li et al. 2022). We follow the methodology outlined in Sunayama et al. (2024) to measure the cluster lensing signal, with two main differences. First, we select source galaxies with a redshift above $z_{l,\,\max} + 0.2$, where $z_{l,\,\max}$ is the maximum redshift of the lenses (i.e. the clusters). We only consider clusters in the redshift range $0.3 < z < 0.7$ as we do not have a large enough sample of clusters or sources to make this measurement at higher redshifts. Within this range, there are 24 miscentred clusters and 72 well-centred clusters. Secondly, we do not include boost and random corrections to the lensing signal. The former corrects for a dilution of the lensing signal due to source galaxies that are physically associated with the lens cluster, and the latter accounts for possible residual systematics in the shape measurement due to imperfect corrections of optical distortion across the field of view of the camera. Given the small sample size of our clusters, the measurement of the corrections is very noisy. Moreover, this paper focuses only on a comparison of lensing signals to identify potential suppression in the signal due to miscentring. Since there is no reason to expect that the corrections will be different for the populations of clusters that we compare (e.g. well-centred versus miscentred), and we are not presenting the measurement of an absolute value of the signal, the corrections are unnecessary for the purposes of this work. For the same reason, we only use the shape-noise covariance matrix, which does not have any covariances between different angular bins.

In Fig. 13, we compare the lensing signals for the well-centred and miscentred clusters (as identified in Section 3.2) in the redshift range $0.3 < z < 0.7$, using the CAMIRA central galaxy as the cluster centre. $\Delta\Sigma(R)$ is the cluster's lensing signal as a function of radius, and $\Delta\Sigma_\times(R)$ is the lensing signal in the 45-degree rotated component. The error bars represent the intrinsic shape noise. For the range of scales that we are interested in, and given the small sample size of our clusters, the shape noise is the dominant source of errors. A non-zero $\Delta\Sigma_\times$ would suggest that there are systematic effects in the lensing signal that must be corrected, but for both the well-centred and miscentred clusters, our measurement of $\Delta\Sigma_\times$ is consistent with zero. The lensing signals of the two samples, shown in the left panel of Fig. 13, are consistent on large scales ($> 2h^{-1}$ Mpc). However, the miscentred clusters show a suppressed signal below $\sim 1h^{-1}$ Mpc relative to the well-centred sample. This is what we would expect if the centroids of those clusters are systematically wrong; i.e. if the clusters are indeed miscentred. In fact, the difference in $\Delta\Sigma(R)$ between the well-centred and miscentred samples is statistically significant – performing a χ^2 test, we find $\chi^2 = 36.6$ with 10 degrees of freedom, giving a p-value of 6.6×10^{-6}. While one could, in principle, explore how this p-value varies as a function of the well-centred cutoff (which we defined in Section 3.2), our results confirm that our selection of the two cluster populations is at least approximately accurate.

We further estimate the impact of miscentring on the lensing signal by comparing the measured lensing signal for both well-centred and

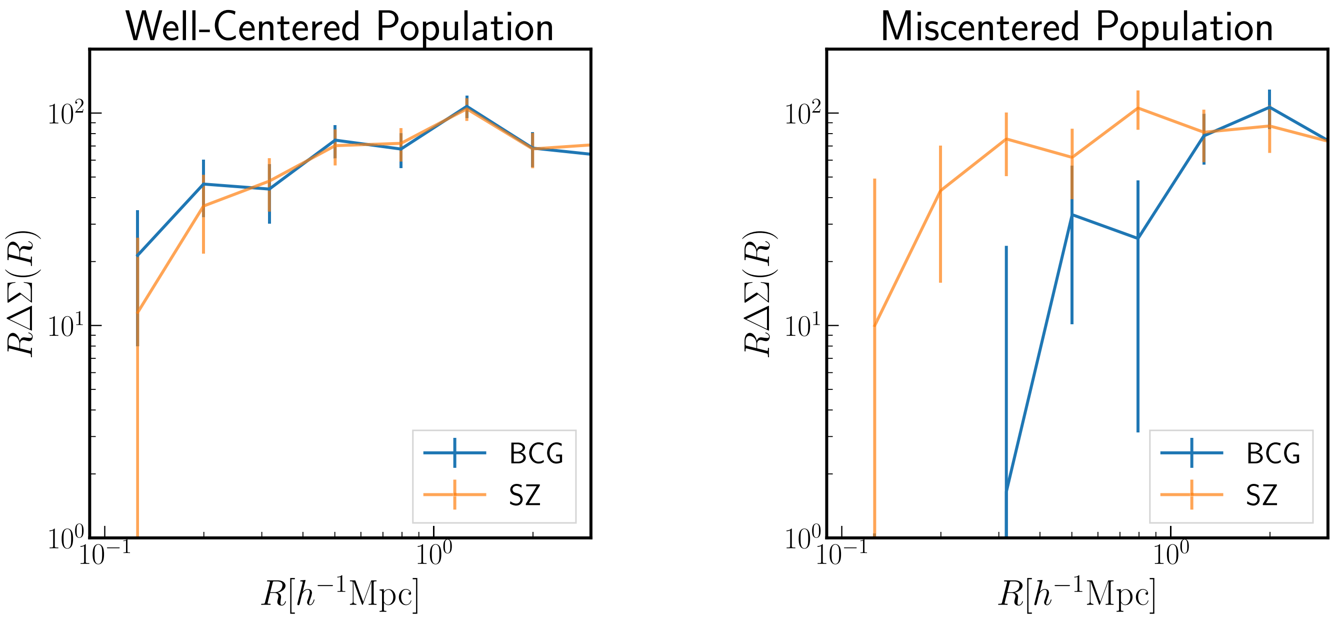

Figure 14. The measured lensing signal $R\Delta\Sigma(R)$ for both well-centred (left) and miscentred (right) clusters using the CAMIRA central galaxy (BCG) as the cluster centre compared to using the ACT SZ centre. These plots use clusters in the redshift range $0.3 < z < 0.7$. For the well-centred population, $\Delta\Sigma(R)$ is consistent regardless of whether the SZ or BCG centre was used in the measurement. For the miscentred population, $\Delta\Sigma(R)$ is significantly suppressed at small scales when using the BCG centre instead of the SZ centre. $\Delta\Sigma(R)$ at the lowest radius is not shown for the miscentred clusters because it is negative with a large error bar. The difference in $\Delta\Sigma(R)$ between the two choices of centres is statistically significant for the miscentred population ($p = 0.0276$) but is not statistically significant for the well-centred population.

miscentred clusters using the CAMIRA central galaxy as the cluster centre, relative to using the ACT SZ centre. These results are shown in Fig. 14 for the well-centred (left panel) and miscentred clusters (right panel) in the redshift range $0.3 < z < 0.7$. For the well-centred population, whether we use BCG or SZ centres to measure $\Delta\Sigma(R)$, we get relatively consistent results. For the SZ centres, however, we see some suppression relative to the BCG centre measurements at the smallest scales measured. Although this suppression is statistically insignificant (we find $\chi^2 = 0.98$ with 10 degrees of freedom, giving a p-value of 0.999843), we believe it could stem from the $\sim$0.15 Mpc positional uncertainty on the SZ centre, as discussed in Section 3.1.

For the miscentred population, we see that the BCG and SZ centre lensing signals are inconsistent with each other. The lensing signals measured using the BCG centre are suppressed at small scales relative to those measured with the SZ centres. The difference in $\Delta\Sigma(R)$ between the two signals is statistically significant – we find $\chi^2 = 20.18$ with 10 degrees of freedom, giving a p-value of 0.027595. This suggests the SZ centres are more likely to represent the true cluster centre than the BCG centres are. This verifies our intuition that, for miscentred clusters, one or more mechanisms cause CAMIRA to place the centre far away from the true BCG, or clusters in the process of merging have BCGs far from the merged cluster centre; in either case, the signal is suppressed. This makes the SZ centre (i.e. the bottom of the gas potential well) more reliable for making lensing measurements.

6 DISCUSSION AND CONCLUSIONS

Utilizing the CAMIRA and ACT cluster catalogues – based on deep optical imaging and the SZ effect in CMB maps, respectively – we constructed a new cross-matched sample of 186 clusters that is larger and deeper than those in many previous miscentring studies. After modelling the distribution of centring offsets in this fiducial sample, we found a miscentred fraction of ~ 25 per cent, a value generally consistent with previous studies. We examined the image of each miscentred cluster in our fiducial sample and identified one of several reasons to explain the miscentring. While some of the miscentred clusters are undergoing mergers, a number of them are miscentred due to non-astrophysical effects: a large fraction of the miscentred clusters can be ascribed to limitations of the HSC data and/or the CAMIRA algorithm, including bright star masks, observational artefacts, and deblending issues. We also found a few clusters that are miscentred due to a false match between HSC and ACT clusters or due to an ACT signal that does not correspond to a real cluster.

In order to further verify our classification of well-centred and miscentred clusters, we computed their weak lensing signals. Compared to well-centred clusters, the miscentred clusters' lensing signal is significantly suppressed, especially at small radii. However, when we computed the miscentred lensing signal with their SZ centres instead of their BCG centres, there was a much clearer signal at small radii. Both of these trends verify our intuition that the BCG centres of miscentred clusters are significantly offset from their true gravitational centres.

We created a cleaned sample of 164 clusters that omits all clusters with clear, non-astrophysical causes of miscentring. The threshold beyond which we define a cluster to be miscentred grows from 330 to 370 kpc, and the inferred miscentred fraction is considerably smaller, ~ 10 per cent. All but one of the clusters for which we were unable to identify a cause for miscentring (Section 4.3.4) fall below the new threshold, affirming the ability of our cleaned offset model to accurately separate clusters into well-centred and miscentred populations.

Additional work is needed to further investigate how both astrophysical processes and systematic effects in cluster-finding algorithms may contribute to miscentring. Bright, radio-emitting galaxies are not exclusively BCGs (Lin & Mohr 2007), so it is plausible that radio sources can cause SZ centres to be less accurate. Indeed, such compact sources are known to contaminate ACT cluster data (Dicker et al. 2021), but whether compact sources can induce significant miscentring of the SZ signal needs further investigation. Meanwhile, from a numerical perspective, one could use cluster hydrodynamical simulations (e.g. Gupta et al. 2017; Yan et al. 2020; Seppi et al. 2023) that compute both a cluster's optical and gas signals. Such an analysis would allow us to study miscentring without observational effects: for example, one could investigate the fraction of merging clusters that have well-defined centres with a fully-formed central galaxy at the bottom of the cluster potential well.

We suggest that future iterations of optical cluster-finding algorithms explicitly account for non-astrophysical causes of miscentring. For example, one could assign a 'miscentring probability' to a cluster based on its proximity to a bright star or observational artefact. One could also develop cluster-finding algorithms that examine optical, X-ray, and/or SZ data simultaneously; such algorithms may reduce the number of false matches between different data sets. Such improvements to optical cluster-finding algorithms may reduce the number of clusters with incorrectly identified optical centres.

By constraining the fraction of clusters that are miscentred due to mergers, one can better understand the history of BCG and cluster formation. Furthermore, one can more precisely correct for miscentring-related biases in cluster lensing analyses for cosmology (McClintock et al. 2019; Zhang et al. 2019). Another implication of our study is that miscentring is an inevitable systematic in cluster lensing studies – due to ongoing mergers, a non-trivial fraction of clusters will lack any well-defined centre. This factor may help motivate cosmological studies that fall outside of conventional cluster cosmology; e.g. studies that derive cosmological parameters from the properties of the most massive galaxies (Xhakaj et al. 2024).

It is worth noting a few miscentring studies which find different miscentred fractions from ours. For example, Willis et al. (2021) find a larger miscentred fraction of ~ 55 per cent; this may be due to the fact that their model finds $\sigma_1 = 60$ kpc, which is considerably smaller than our adopted $\sigma_1 = 150$ kpc. Meanwhile, Kelly et al. (2024) find a smaller miscentred fraction of $\sim 10-20$ per cent. Furthermore, Seppi et al. (2023) uses a different classification system altogether, categorizing clusters as dynamically *relaxed* or *disturbed* instead of well-centred or miscentred, respectively; they find a disturbed fraction of 69 per cent. Therefore, it is worthwhile to perform additional miscentring studies in order to place stronger constraints on $f_{\rm cen}$. Although previous studies have used a two-component model, future studies could explore more complex models; in reality, the division of well-centred and miscentred populations may not be cleanly bimodal.

With future data releases from HSC and ACT, even larger cross-matched samples can be built to study miscentring. Outside of these two surveys, one might also use upcoming data from the Vera C. Rubin Observatory (Ivezić et al. 2019), which will be deeper and cover a much larger footprint on the sky; and *eROSITA* (Liu et al. 2022), which is mapping the entire sky in X-rays.

ACKNOWLEDGEMENTS

We would like to thank Eduardo Rozo, Tesla Jeltema, Neelima Sehgal, Ed Wollack, and Bruce Partridge for helpful discussions and suggestions. RD acknowledges support from the NSF Graduate Research Fellowship Program under Grant No. DGE-2039656. MH acknowledges support from the National Research Foundation of South Africa. CS acknowledges support from the Agencia Nacional de Investigación y Desarrollo (ANID) through Basal project FB210003.

The Hyper Suprime-Cam (HSC) collaboration includes the astronomical communities of Japan and Taiwan, and Princeton University. The HSC instrumentation and software were developed by the National Astronomical Observatory of Japan (NAOJ), the Kavli Institute for the Physics and Mathematics of the Universe (Kavli IPMU), the University of Tokyo, the High Energy Accelerator Research Organization (KEK), the Academia Sinica Institute for Astronomy and Astrophysics in Taiwan (ASIAA), and Princeton University. Funding was contributed by the FIRST programme from the Japanese Cabinet Office, the Ministry of Education, Culture, Sports, Science and Technology (MEXT), the Japan Society for the Promotion of Science (JSPS), Japan Science and Technology Agency (JST), the Toray Science Foundation, NAOJ, Kavli IPMU, KEK, ASIAA, and Princeton University.

This paper makes use of software developed for Vera C. Rubin Observatory. We thank the Rubin Observatory for making their code available as free software at http://pipelines.lsst.io/.

This paper is based on data collected at the Subaru Telescope and retrieved from the HSC data archive system, which is operated by the Subaru Telescope and Astronomy Data Center (ADC) at NAOJ. Data analysis was in part carried out with the cooperation of Center for Computational Astrophysics (CfCA), NAOJ. We are honored and grateful for the opportunity of observing the Universe from Maunakea, which has the cultural, historical, and natural significance in Hawaii.

The Pan-STARRS1 Surveys (PS1) and the PS1 public science archive have been made possible through contributions by the Institute for Astronomy, the University of Hawaii, the Pan-STARRS Project Office, the Max Planck Society and its participating institutes, the Max Planck Institute for Astronomy, Heidelberg, and the Max Planck Institute for Extraterrestrial Physics, Garching, The Johns Hopkins University, Durham University, the University of Edinburgh, the Queen's University Belfast, the Harvard-Smithsonian Center for Astrophysics, the Las Cumbres Observatory Global Telescope Network Incorporated, the National Central University of Taiwan, the Space Telescope Science Institute, the National Aeronautics and Space Administration under grant No. NNX08AR22G issued through the Planetary Science Division of the NASA Science Mission Directorate, the National Science Foundation grant No. AST-1238877, the University of Maryland, Eotvos Lorand University (ELTE), the Los Alamos National Laboratory, and the Gordon and Betty Moore Foundation.

Support for ACT was through the U.S. National Science Foundation through awards AST-0408698, AST-0965625, and AST-1440226 for the ACT project, as well as awards PHY-0355328, PHY-0855887 and PHY-1214379. Funding was also provided by Princeton University, the University of Pennsylvania, and a Canada Foundation for Innovation (CFI) award to UBC. ACT operated in the Parque Astronómico Atacama in northern Chile under the auspices of the Agencia Nacional de Investigación y Desarrollo (ANID). The development of multichroic detectors and lenses was supported by NASA grants NNX13AE56G and NNX14AB58G. Detector research at NIST was supported by the NIST Innovations in Measurement Science programme. Computing for ACT was performed using the Princeton Research Computing resources at Princeton University, the

National Energy Research Scientific Computing Center (NERSC), and the Niagara supercomputer at the SciNet HPC Consortium. SciNet is funded by the CFI under the auspices of Compute Canada, the Government of Ontario, the Ontario Research Fund–Research Excellence, and the University of Toronto. We thank the Republic of Chile for hosting ACT in the northern Atacama, and the local indigenous Licanantay communities whom we follow in observing and learning from the night sky.

DATA AVAILABILITY

The HSC optical catalogue used in this paper can be found at https://github.com/oguri/cluster_catalogues/tree/main/hsc_s19a_camira, while the ACT SZ catalogue can be found at https://lambda.gsfc.nasa.gov/product/act/actpol_dr5_szcluster_catalog_get.html. We will provide our fiducial cross-matched catalogue upon request.

REFERENCES

Abbott T. M. C. et al., 2018, ApJS, 239, 18
Abbott T. M. C. et al., 2020, Phys. Rev. D, 102, 023509
Ahn C. P. et al., 2012, ApJS, 203, 21
Ahumada R. et al., 2020, ApJS, 249, 3
Aihara H. et al., 2018, PASJ, 70, S4
Aihara H. et al., 2022, PASJ, 74, 247
Allen S. W., Evrard A. E., Mantz A. B., 2011, ARA&A, 49, 409
Astropy Collaboration 2022, ApJ, 935, 167
Bahcall N. A., Fan X., 1998, ApJ, 504, 1
Binney J., Tremaine S., 2008, Galactic Dynamics, 2nd edn. Princeton Univ. Press, Princeton
Bleem L. E. et al., 2020, ApJS, 247, 25
Bosch J. et al., 2018, PASJ, 70, S5
Chandrasekhar S., 1943, ApJ, 97, 255
Clerc N., Finoguenov A., 2023, in Bambi C., Santangelo A., eds, Handbook of X-ray and Gamma-ray Astrophysics. Springer, Singapore, p. 123
Coupon J., Czakon N., Bosch J., Komiyama Y., Medezinski E., Miyazaki S., Oguri M., 2018, PASJ, 70, S7
Dalal R., Strauss M. A., Sunayama T., Oguri M., Lin Y.-T., Huang S., Park Y., Takada M., 2021, MNRAS, 507, 4016
Dey A. et al., 2019, AJ, 157, 168
Dicker S. R. et al., 2021, MNRAS, 508, 2600
Ebeling H., Edge A. C., Bohringer H., Allen S. W., Crawford C. S., Fabian A. C., Voges W., Huchra J. P., 1998, MNRAS, 301, 881
Faltenbacher A., Gottloeber S., Mathews W. G., 2006, preprint (astro–ph/0609615)
Gaia Collaboration 2023, A&A, 674, A1
Gaia Collaboration, 2022, VizieR Online Data Catalog, I/355
Garrel C. et al., 2022, A&A, 663, A3
Gladders M. D., Yee H. K. C., 2005, ApJS, 157, 1
Grandis S. et al., 2021, MNRAS, 504, 1253
Gupta N., Saro A., Mohr J. J., Dolag K., Liu J., 2017, MNRAS, 469, 3069
Hausman M. A., Ostriker J. P., 1978, ApJ, 224, 320
Hilton M. et al., 2021, ApJS, 253, 3
Hilton M. et al., 2023a, Astrophysics Source Code Library, record ascl:2308.006
Hilton M., Kesebonye K., Phakathi P., Pillay D., Ragavan D., 2023b, Astrophysics Source Code Library, record ascl:2310.007
Hoessel J. G., Schneider D. P., 1985, AJ, 90, 1648
Hollowood D. L. et al., 2019, ApJS, 244, 22
Huang S., Leauthaud A., Greene J. E., Bundy K., Lin Y.-T., Tanaka M., Miyazaki S., Komiyama Y., 2018, MNRAS, 475, 3348
Ivezić Ž. et al., 2019, ApJ, 873, 111
Kawanomoto S. et al., 2018, PASJ, 70, 66
Kelly P. et al., 2024, Monthly Notices of the Royal Astronomical Society, 533, 1,572–588
Kim R. S. J. et al., 2002, AJ, 123, 20
Kravtsov A. V., Borgani S., 2012, ARA&A, 50, 353
Lauer T. R., Postman M., Strauss M. A., Graves G. J., Chisari N. E., 2014, ApJ, 797, 82
Li X. et al., 2022, PASJ, 74, 421
Lin Y.-T., Mohr J. J., 2007, ApJS, 170, 71
Liu A. et al., 2022, A&A, 661, A2
Machado R. E. G., Monteiro-Oliveira R., Lima Neto G. B., Cypriano E. S., 2015, MNRAS, 451, 3309
Mantz A. B. et al., 2015, MNRAS, 446, 2205
McClintock T. et al., 2019, MNRAS, 482, 1352
Miyazaki S. et al., 2018, PASJ, 70, S1
Naess S. et al., 2020, J. Cosmol. Astropart. Phys., 2020, 046
Oguri M. et al., 2018, PASJ, 70, S20
Oguri M., 2014, MNRAS, 444, 147
Okabe N. et al., 2019, PASJ, 71, 79
Ostriker J. P., Tremaine S. D., 1975, ApJ, 202, L113
Pacaud F. et al., 2007, MNRAS, 382, 1289
Postman M., Lauer T. R., 1995, ApJ, 440, 28
Price-Whelan A. M. et al., 2018, AJ, 156, 123
Robitaille T. P. et al., 2013, A&A, 558, A33
Rozo E. et al., 2010, ApJ, 708, 645
Rykoff E. S. et al., 2014, ApJ, 785, 104
Rykoff E. S. et al., 2016, ApJS, 224, 1
Sehgal N. et al., 2013, ApJ, 767, 38
Seppi R. et al., 2023, A&A, 671, A57
Sunayama T. et al., 2024, Physical Review D, 110, 083511
Sunyaev R. A., Zeldovich Y. B., 1972, Comments Astrophys. Space Phys., 4, 173
Weinberg D. H., Mortonson M. J., Eisenstein D. J., Hirata C., Riess A. G., Rozo E., 2013, Phys. Rep., 530, 87
Willis J. P. et al., 2021, MNRAS, 503, 5624
Wright A. H. et al., 2019, A&A, 632, A34
Xhakaj E., Leauthaud A., Lange J., Krause E., Hearin A., Huang S., Wechsler R. H., Heydenreich S., 2024, MNRAS, 530, 4203
Yan Z., Raza N., Van Waerbeke L., Mead A. J., McCarthy I. G., Tröster T., Hinshaw G., 2020, MNRAS, 493, 1120
Yang X., Mo H. J., van den Bosch F. C., Pasquali A., Li C., Barden M., 2007, ApJ, 671, 153
Zhang Y. et al., 2019, MNRAS, 487, 2578

APPENDIX A: LIST OF CLUSTERS IN FIDUCIAL CROSS-MATCH

We provide a full list of clusters in our fiducial cross-match in Table A1, including their HSC and ACT positions, redshifts, richnesses, SZ signal-to-noise ratios, measured offsets, whether they are miscentred and/or merging, and the cause of the miscentring.

Table A1. The full list of clusters used in our fiducial cross-match. All coordinates are listed in degrees. The values for redshift (z) and richness (λ) are taken from the HSC catalogue, SNR refers to the ACT SNR, r is the centring offset, 'Miscent.'? indicates if the cluster is miscentred (see Section 3.2), 'Merging'? indicates if the cluster is merging (see Section 4.1), and 'Cause of miscent'. indicates the cause of miscentring (see Section 4).

HSC name	HSC RA (°)	HSC dec (°)	ACT name	ACT RA (°)	ACT dec (°)	z	λ	SNR	r (Mpc)	Miscent.?	Merging?	Cause of miscent.
HSCJ000217+013157	0.570211	1.532472	ACT-CL J0002.3+0131	0.583333	1.524909	0.81	34.607	4.615	0.411	True	False	Multiple possible
HSCJ000350+020359	0.956952	2.066506	ACT-CL J0003.8+0203	0.954179	2.06261	0.1142	31.927	5.491	0.0357	False	False	N/A
HSCJ000500+021143	1.249243	2.195339	ACT-CL J0005.0+0212	1.251648	2.201674	0.827	25.975	5.04	0.1852	False	False	N/A
HSCJ000547+022256	1.44459	2.382173	ACT-CL J0005.7+0222	1.441633	2.370831	0.8167	24.325	4.845	0.319	False	False	N/A
HSCJ000634+001806	1.641751	0.301708	ACT-CL J0006.5+0017	1.643564	0.285975	0.698	30.785	5.507	0.4069	True	False	Misidentified CG
HSCJ000654-004120	1.725384	−0.688763	ACT-CL J0006.9−0041	1.730549	−0.686201	0.5552	59.479	9.08	0.1337	False	True	N/A
HSCJ000810+020112	2.043308	2.0201	ACT-CL J0008.1+0201	2.045439	2.019734	0.354	70.37	15.931	0.0387	False	True	N/A
HSCJ015654−042426	29.226423	−4.407102	ACT-CL J0156.8−0424	29.222169	−4.405736	0.138	30.982	4.744	0.0391	False	False	N/A
HSCJ015826−014639	29.607963	−1.777593	ACT-CL J0158.4−0145	29.603343	−1.763265	0.1625	54.471	5.527	0.1514	False	False	N/A
HSCJ015913−032420	29.802687	−3.405454	ACT-CL J0159.2−0324	29.812338	−3.408333	0.5407	22.081	4.422	0.2301	False	False	N/A
HSCJ015921−030955	29.839286	−3.165221	ACT-CL J0159.3−0310	29.829256	−3.170783	0.622	20.469	4.719	0.2803	False	False	N/A
HSCJ015931−035023	29.877133	−3.839823	ACT-CL J0159.4−0350	29.874309	−3.839241	0.7799	67.619	5.754	0.0771	False	False	N/A
HSCJ020147−021154	30.445168	−2.198314	ACT-CL J0201.6−0211	30.423806	−2.198919	0.204	72.431	9.219	0.2576	False	True	N/A
HSCJ020300−004236	30.748478	−0.709983	ACT-CL J0203.0−0042	30.751043	−0.707206	0.4246	31.269	5.34	0.0758	False	False	N/A
HSCJ020317−012401	30.819173	−1.40022	ACT-CL J0203.2−0123	30.815637	−1.396675	0.7011	28.334	6.107	0.1289	False	True	N/A
HSCJ020447−011713	31.196516	−1.287044	ACT-CL J0204.7−0116	31.190626	−1.28232	0.312	29.098	4.717	0.1244	False	False	N/A
HSCJ020456−030321	31.232113	−3.055755	ACT-CL J0204.8−0303	31.209438	−3.06144	0.5479	25.113	10.422	0.5378	True	False	Star
HSCJ020517−043920	31.319592	−4.655573	ACT-CL J0205.2−0439	31.317053	−4.653123	0.96	39.663	12.089	0.1005	False	True	N/A
HSCJ020613−011500	31.554741	−1.250012	ACT-CL J0206.2−0114	31.556563	−1.242799	0.6834	60.863	14.43	0.1895	False	True	N/A
HSCJ020623−011832	31.595229	−1.308775	ACT-CL J0206.4−0118	31.608295	−1.308362	0.1955	39.762	4.823	0.1525	False	False	N/A
HSCJ020658−011951	31.743357	−1.330933	ACT-CL J0206.9−0119	31.737571	−1.333333	0.5411	24.372	4.463	0.1434	False	True	N/A
HSCJ020816−023724	32.067082	−2.62341	ACT-CL J0208.2−0237	32.064946	−2.621668	0.5124	35.454	5.581	0.0613	False	False	N/A
HSCJ020820−025608	32.081581	−2.935489	ACT-CL J0208.3−0255	32.085929	−2.93323	0.946	26.834	5.658	0.1392	False	False	N/A
HSCJ021002−024411	32.507873	−2.736408	ACT-CL J0210.0−0243	32.504257	−2.720847	0.658	23.021	4.609	0.4006	True	False	Deblending
HSCJ021056−061154	32.735023	−6.198431	ACT-CL J0210.9−0611	32.737387	−6.193518	0.4315	43.368	5.797	0.1102	False	True	N/A
HSCJ021102−045318	32.757776	−4.88833	ACT-CL J0211.1−0453	32.8	−4.895703	0.144	15.437	4.655	0.3885	True	False	False match
HSCJ021115−034324	32.811752	−3.723309	ACT-CL J0211.2−0343	32.811616	−3.723237	0.7536	62.216	8.936	0.0041	False	False	N/A
HSCJ021321−060437	33.337991	−6.076813	ACT-CL J0213.3−0605	33.337377	−6.099905	0.702	48.262	6.518	0.5949	True	False	Multiple possible
HSCJ021426−062740	33.607429	−6.461161	ACT-CL J0214.4−0628	33.613948	−6.467543	0.2308	50.971	5.219	0.1206	False	False	N/A
HSCJ021441−043402	33.671241	−4.567356	ACT-CL J0214.7−0432	33.67881	−4.548587	0.1485	68.543	4.554	0.1888	False	True	N/A
HSCJ021528−044041	33.867653	−4.678115	ACT-CL J0215.4−0440	33.866667	−4.670873	0.356	41.609	4.435	0.1314	False	False	N/A
HSCJ021835−011434	34.644288	−1.242899	ACT-CL J0218.5−0114	34.64254	−1.242802	0.868	40.461	5.742	0.0486	False	False	N/A
HSCJ022056−033348	35.231588	−3.563314	ACT-CL J0220.9−0332	35.236988	−3.547877	1.0139	36.94	5.137	0.4729	True	False	Multiple possible

Table A1 – *continued*

HSC name	HSC RA (°)	HSC dec (°)	ACT name	ACT RA (°)	ACT dec (°)	z	λ	SNR	r (Mpc)	Miscent.?	Merging?	Cause of miscent.
HSCJ022146−034619	35.440625	−3.771928	ACT-CL J0221.7−0346	35.439659	−3.772847	0.42	82.458	10.414	0.0265	False	True	N/A
HSCJ022156−034054	35.481354	−3.68159	ACT-CL J0221.9−0340	35.481415	−3.669552	1.052	32.01	6.229	0.351	True	True	Merger
HSCJ022528−035502	36.364613	−3.917308	ACT-CL J0225.4−0355	36.366797	−3.933333	0.7846	27.499	4.564	0.4342	True	False	False signal
HSCJ022738−031757	36.909256	−3.299209	ACT-CL J0227.6−0318	36.911256	−3.30087	0.847	54.071	6.824	0.0715	False	False	N/A
HSCJ022936−033623	37.401047	−3.606418	ACT-CL J0229.6−0336	37.410493	−3.611185	0.316	37.784	6.913	0.1755	False	True	N/A
HSCJ023141−045257	37.921574	−4.882613	ACT-CL J0231.7−0453	37.935949	−4.886	0.187	117.669	9.247	0.1658	False	True	N/A
HSCJ023217−061914	38.070717	−6.320418	ACT-CL J0232.2−0617	38.052728	−6.294417	1.1521	22.545	4.289	0.9361	True	True	Merger
HSCJ023336−053022	38.398282	−5.506037	ACT-CL J0233.6−0530	38.405235	−5.508124	0.4296	49.864	8.612	0.1459	False	True	N/A
HSCJ023516−032348	38.816422	−3.396777	ACT-CL J0235.2−0323	38.808404	−3.387505	0.578	42.807	4.682	0.2897	False	True	N/A
HSCJ023643−022953	39.180914	−2.497939	ACT-CL J0236.7−0228	39.179107	−2.470875	0.604	18.859	4.763	0.6548	True	False	Artifact
HSCJ023655−060708	39.228944	−6.11882	ACT-CL J0236.8−0607	39.224926	−6.125074	0.688	24.131	5.467	0.1896	False	True	N/A
HSCJ083932−014128	129.884537	−1.691122	ACT-CL J0839.5−0140	129.876467	−1.676617	0.2605	47.413	6.536	0.2408	False	False	N/A
HSCJ084225+003236	130.602173	0.54322	ACT-CL J0842.3+0033	130.595658	0.554184	1.028	36.414	4.78	0.37	True	True	Merger
HSCJ084441+021656	131.171072	2.282303	ACT-CL J0844.6+0216	131.170545	2.276926	0.6404	69.556	5.256	0.1339	False	False	N/A
HSCJ084502+012631	131.259589	1.442025	ACT-CL J0845.0+0127	131.25981	1.46531	0.4165	29.912	5.858	0.4615	True	False	Multiple possible
HSCJ084526+032732	131.35941	3.458953	ACT-CL J0845.4+0327	131.36915	3.462576	0.322	69.067	12.237	0.1746	False	False	N/A
HSCJ084824+041206	132.098806	4.201732	ACT-CL J0848.4+0412	132.105052	4.204553	0.8533	58.139	6.005	0.1888	False	False	N/A
HSCJ084831−012137	132.127353	−1.360332	ACT-CL J0848.5−0122	132.13888	−1.367742	0.616	16.443	4.903	0.3337	True	True	Merger
HSCJ084939−005121	132.413654	−0.855933	ACT-CL J0849.6−0051	132.416562	−0.854322	0.616	50.99	5.684	0.081	False	True	N/A
HSCJ085132+045227	132.881637	4.874083	ACT-CL J0851.5+0452	132.888864	4.880626	0.4	33.919	4.36	0.1882	False	False	N/A
HSCJ085221−010047	133.086607	−1.012999	ACT-CL J0852.2−0101	133.070604	−1.020816	0.438	39.217	7.313	0.3635	True	True	Star
HSCJ085450−012157	133.706648	−1.365851	ACT-CL J0854.7−0122	133.695815	−1.37217	0.3428	27.248	5.195	0.22	False	False	N/A
HSCJ085530−010656	133.875864	−1.115507	ACT-CL J0855.4−0106	133.869549	−1.115603	0.7491	39.263	5.664	0.1668	False	True	N/A
HSCJ085622+014656	134.092204	1.782199	ACT-CL J0856.3+0146	134.086063	1.783076	0.7636	34.7	8.662	0.1649	False	False	N/A
HSCJ085629+014431	134.122187	1.741871	ACT-CL J0856.5+0143	134.128276	1.7257	0.7067	49.379	6.504	0.4462	True	True	Star
HSCJ085754+031035	134.474797	3.176485	ACT-CL J0857.8+0310	134.46401	3.178078	0.192	61.529	11.373	0.1252	False	True	N/A
HSCJ085903−012004	134.760998	−1.334328	ACT-CL J0859.0−0119	134.75414	−1.333333	1.336	26.834	4.638	0.2095	False	False	N/A
HSCJ085932+030841	134.884675	3.144733	ACT-CL J0859.4+0308	134.875	3.14588	0.186	26.059	4.14	0.1091	False	True	N/A
HSCJ090119+030156	135.330628	3.03219	ACT-CL J0901.5+0301	135.385139	3.019336	0.194	42.298	4.844	0.6487	True	True	Star
HSCJ090141−013648	135.420606	−1.613274	ACT-CL J0901.5−0139	135.375769	−1.66332	0.3031	25.609	5.671	1.085	True	True	Artifact
HSCJ090330−013622	135.875628	−1.606151	ACT-CL J0903.4−0136	135.871684	−1.603024	0.4448	43.979	5.458	0.1036	False	False	N/A
HSCJ090419+020641	136.079294	2.111412	ACT-CL J0904.3+0206	136.079874	2.106649	0.8076	28.802	4.698	0.1301	False	False	N/A
HSCJ090754+005732	136.976449	0.958979	ACT-CL J0907.8+0057	136.971935	0.953086	0.686	31.757	5.153	0.1894	False	True	N/A
HSCJ090756+025422	136.981336	2.906203	ACT-CL J0907.9+0254	136.983333	2.912502	0.8073	46.372	4.106	0.1791	False	False	N/A
HSCJ090932−005016	137.385315	−0.837881	ACT-CL J0909.5−0050	137.383377	−0.835399	1.09	38.623	4.606	0.0925	False	True	N/A
HSCJ091449+001018	138.704735	0.171563	ACT-CL J0914.7+0011	138.695729	0.191667	0.5414	18.816	4.253	0.5045	True	False	Star
HSCJ091555−013244	138.981014	−1.545651	ACT-CL J0915.9−0132	138.989099	−1.545581	0.5	33.561	5.778	0.1776	False	True	N/A
HSCJ091606−002338	139.023871	−0.393884	ACT-CL J0916.1−0024	139.04253	−0.401908	0.288	60.628	10.714	0.3165	False	True	N/A
HSCJ091850+021203	139.709235	2.200894	ACT-CL J0918.7+0211	139.686703	2.190027	0.266	54.374	4.464	0.3682	True	True	Merger
HSCJ092024+013444	140.098056	1.578875	ACT-CL J0920.4+0134	140.100017	1.577392	0.68	51.074	5.61	0.0625	False	False	N/A
HSCJ092121+031713	140.337964	3.286995	ACT-CL J0921.3+0317	140.335619	3.288125	0.3513	105.961	10.708	0.0463	False	True	N/A
HSCJ092211+034641	140.545649	3.77819	ACT-CL J0922.1+0346	140.533808	3.773285	0.25	65.172	5.249	0.1801	False	True	N/A

Table A1 – *continued*

HSC name	HSC RA (°)	HSC dec (°)	ACT name	ACT RA (°)	ACT dec (°)	z	λ	SNR	r (Mpc)	Miscent.?	Merging?	Cause of miscent.
HSCJ093512+004932	143.801208	0.825611	ACT-CL J0935.2+0048	143.80869	0.800777	0.3521	78.408	13.913	0.463	True	True	Merger
HSCJ093523+023325	143.843843	2.556878	ACT-CL J0935.3+0233	143.842726	2.551368	0.5214	46.617	11.436	0.1263	False	True	N/A
HSCJ094345+005916	145.936227	0.987781	ACT-CL J0943.7+0059	145.947342	0.988996	0.4343	34.384	4.681	0.2271	False	True	N/A
HSCJ094747−013154	146.94549	−1.531617	ACT-CL J0947.7−0132	146.94504	−1.534906	0.882	30.164	5.069	0.0926	False	False	N/A
HSCJ094759−011941	146.994134	−1.328169	ACT-CL J0947.9−0120	146.992928	−1.334111	1.1041	54.343	13.207	0.1785	False	True	N/A
HSCJ095140−001420	147.917065	−0.238932	ACT-CL J0951.6−0014	147.921976	−0.239948	0.4271	45.255	9.527	0.1009	False	False	N/A
HSCJ095612+015935	149.04878	1.992959	ACT-CL J0956.1+0158	149.044615	1.980276	0.946	43.346	5.947	0.3796	True	True	Merger
HSCJ100452−013748	151.214658	−1.629998	ACT-CL J1004.8−0137	151.212664	−1.629311	0.3017	25.549	5.475	0.0339	False	True	N/A
HSCJ100532+023518	151.381352	2.588443	ACT-CL J1005.5+0235	151.383407	2.585845	0.372	49.045	4.741	0.0612	False	False	N/A
HSCJ100944+025413	152.43191	2.903656	ACT-CL J1009.7+0255	152.428211	2.926406	0.382	39.706	6.556	0.4333	True	False	Multiple possible
HSCJ101229+023958	153.122707	2.666196	ACT-CL J1012.5+0239	153.129263	2.662599	0.24	81.221	8.224	0.102	False	True	N/A
HSCJ101402+023754	153.509016	2.631569	ACT-CL J1014.0+0237	153.504148	2.625	0.5773	27.166	4.126	0.1932	False	True	N/A
HSCJ101407+003827	153.530422	0.64089	ACT-CL J1014.1+0038	153.529466	0.642712	1.2433	44.502	10.402	0.0617	False	False	N/A
HSCJ101443+031037	153.679031	3.176877	ACT-CL J1014.6+0310	153.666752	3.180976	0.7381	34.751	4.643	0.3395	True	True	Merger
HSCJ101846−013103	154.690919	−1.517421	ACT-CL J1018.7−0130	154.692935	−1.516609	0.3953	29.722	6.614	0.0417	False	True	N/A
HSCJ102006−001306	155.025417	−0.218415	ACT-CL J1020.1−0013	155.027719	−0.219368	0.3939	57.07	4.577	0.0477	False	False	N/A
HSCJ102750+000328	156.957222	0.057738	ACT-CL J1027.8+0004	156.958334	0.06895	0.714	27.956	5.27	0.2921	False	False	N/A
HSCJ102956+001650	157.483609	0.280606	ACT-CL J1029.9+0016	157.478109	0.277933	1.347	27.972	6.001	0.1851	False	False	N/A
HSCJ103112+003130	157.800549	0.525109	ACT-CL J1031.2+0031	157.808297	0.529233	0.8811	17.087	4.88	0.2447	False	False	N/A
HSCJ103525−000141	158.855791	−0.028051	ACT-CL J1035.4−0001	158.85925	−0.032014	0.4824	68.922	5.859	0.1134	False	True	N/A
HSCJ104713−011612	161.806053	−1.270103	ACT-CL J1047.2−0116	161.802374	−1.270221	0.7439	43.676	4.73	0.0969	False	True	N/A
HSCJ104723−010430	161.847253	−1.074965	ACT-CL J1047.4−0103	161.850941	−1.065627	0.478	26.515	5.327	0.2153	False	False	N/A
HSCJ105040+001707	162.666271	0.285331	ACT-CL J1050.6+0017	162.667243	0.284428	0.59	28.162	7.019	0.0317	False	False	N/A
HSCJ110728+012138	166.867214	1.360674	ACT-CL J1107.4+0121	166.860813	1.35588	0.5872	47.358	5.122	0.1905	False	True	N/A
HSCJ111017−003023	167.572548	−0.506422	ACT-CL J1110.2−0030	167.573192	−0.504919	0.9954	31.428	5.167	0.0471	False	True	N/A
HSCJ111111+004508	167.796717	0.752179	ACT-CL J1111.1+0044	167.798448	0.748426	0.1971	49.759	5.667	0.0485	False	True	N/A
HSCJ111654−003648	169.223668	−0.613324	ACT-CL J1116.9−0036	169.228957	−0.612512	0.8338	45.79	4.687	0.1466	False	False	N/A
HSCJ111846+003851	169.691587	0.647626	ACT-CL J1118.7+0039	169.691618	0.659881	0.588	40.423	5.58	0.2922	False	False	N/A
HSCJ112549+001017	171.452369	0.171272	ACT-CL J1125.7+0010	171.431499	0.178289	0.748	42.912	4.855	0.5811	True	True	Merger
HSCJ112733+000342	171.885477	0.061779	ACT-CL J1127.5+0003	171.891548	0.066667	1.3641	17.599	4.159	0.2361	False	False	N/A
HSCJ112818−005900	172.07378	−0.983255	ACT-CL J1128.3−0058	172.075036	−0.981827	0.468	72.298	6.399	0.0403	False	True	N/A
HSCJ113139−010718	172.913695	−1.121702	ACT-CL J1131.6−0107	172.91175	−1.123247	0.321	68.464	5.912	0.0417	False	False	N/A
HSCJ113408+011536	173.532139	1.259885	ACT-CL J1134.0+0116	173.512546	1.27917	0.736	31.233	5.013	0.7211	True	True	Merger
HSCJ113654+000643	174.226799	0.112083	ACT-CL J1136.9+0006	174.231486	0.100596	0.59	79.803	14.27	0.2963	False	True	N/A
HSCJ113833−001137	174.639459	−0.193605	ACT-CL J1138.5−0011	174.638836	−0.197338	0.8821	47.315	4.417	0.1055	False	False	N/A
HSCJ113919+015412	174.827091	1.903244	ACT-CL J1139.3+0154	174.831111	1.904592	1.0527	36.16	8.141	0.1236	False	False	N/A
HSCJ114409+044133	176.039345	4.692382	ACT-CL J1144.0+0440	176.025	4.679106	0.4093	16.596	4.129	0.3827	True	False	False match
HSCJ114416+022722	176.068573	2.456173	ACT-CL J1144.2+0227	176.054194	2.462539	0.6512	45.159	4.652	0.3923	True	True	Merger
HSCJ114507−010032	176.280823	−1.008907	ACT-CL J1145.1−0100	176.287483	−1.004184	0.6999	30.793	4.186	0.21	False	False	N/A
HSCJ115216+003055	178.066216	0.51537	ACT-CL J1152.2+0031	178.056037	0.523485	0.4597	80.716	8.073	0.2732	False	True	N/A
HSCJ115235+035641	178.145684	3.944594	ACT-CL J1152.5+0356	178.144056	3.94412	0.708	46.783	9.799	0.0437	False	True	N/A
HSCJ115328+025849	178.368111	2.980402	ACT-CL J1153.4+0259	178.370846	2.987527	0.72	19.31	5.107	0.1985	False	True	N/A
HSCJ115417+022126	178.571393	2.357235	ACT-CL J1154.2+0221	178.56668	2.360253	0.7266	43.832	10.862	0.146	False	True	N/A
HSCJ115823+022806	179.593864	2.468256	ACT-CL J1158.3+0228	179.597372	2.470706	0.49	25.459	8.518	0.093	False	False	N/A
HSCJ120054−012826	180.224356	−1.473969	ACT-CL J1200.9−0125	180.231264	−1.433293	0.246	22.295	4.445	0.5739	True	True	Merger
HSCJ120350+012523	180.958005	1.423187	ACT-CL J1203.9+0126	180.9872	1.438063	0.4181	42.186	7.641	0.6507	True	True	Star
HSCJ120533+021425	181.386577	2.240404	ACT-CL J1205.5+0214	181.383333	2.245762	0.7747	41.578	4.347	0.1674	False	True	N/A

Table A1 – *continued*

HSC name	HSC RA (°)	HSC dec (°)	ACT name	ACT RA (°)	ACT dec (°)	z	λ	SNR	r (Mpc)	Miscent.?	Merging?	Cause of miscent.
HSCJ120827+025640	182.113731	2.944318	ACT-CL J1208.3+0254	182.087571	2.916667	0.7909	20.104	4.37	1.0242	True	False	Multiple possible
HSCJ121018+022344	182.573797	2.395467	ACT-CL J1210.2+0223	182.574889	2.391678	0.3942	28.761	6.012	0.0756	False	False	N/A
HSCJ121015+032116	182.564078	3.354489	ACT-CL J1210.2+0321	182.55591	3.364153	1.0324	42.004	6.952	0.3672	True	False	None apparent
HSCJ121322+033226	183.340625	3.540642	ACT-CL J1213.4+0331	183.356343	3.529743	0.3312	17.78	5.07	0.3276	False	True	N/A
HSCJ121340+035120	183.418209	3.855565	ACT-CL J1213.6+0351	183.416808	3.854246	0.8659	37.534	5.163	0.0533	False	True	N/A
HSCJ121832+023328	184.633529	2.557662	ACT-CL J1218.5+0233	184.62618	2.554919	0.768	59.801	9.37	0.2088	False	False	N/A
HSCJ122226−012712	185.610265	−1.45325	ACT-CL J1222.4−0127	185.608345	−1.452562	0.294	44.692	5.206	0.0322	False	True	N/A
HSCJ122422+021211	186.091575	2.20301	ACT-CL J1224.3+0211	186.079273	2.199995	0.4444	63.077	4.899	0.2606	False	False	N/A
HSCJ123835−000359	189.646202	−0.066417	ACT-CL J1238.5−0004	189.643246	−0.066732	0.588	36.675	5.26	0.0709	False	False	N/A
HSCJ124100+001101	190.250186	0.183654	ACT-CL J1241.0+0010	190.255022	0.176655	0.7904	33.969	4.426	0.229	False	False	N/A
HSCJ125036+003646	192.64933	0.612847	ACT-CL J1250.6+0036	192.651492	0.601483	0.6851	56.503	4.821	0.295	False	False	N/A
HSCJ125825+004417	194.603949	0.738087	ACT-CL J1258.4+0043	194.620819	0.733333	0.4	31.104	4.666	0.339	True	False	None apparent
HSCJ131131−011933	197.880946	−1.325761	ACT-CL J1311.5−0119	197.878621	−1.33201	0.1836	111.773	24.339	0.074	False	False	N/A
HSCJ131504+012113	198.766517	1.353512	ACT-CL J1315.0+0121	198.766667	1.354123	0.738	32.825	4.179	0.0165	False	True	N/A
HSCJ134614−014307	206.557026	−1.718662	ACT-CL J1346.2−0142	206.558458	−1.71314	1.1899	55.088	6.26	0.1701	False	True	N/A
HSCJ134745+012410	206.936073	1.402849	ACT-CL J1347.7+0124	206.936216	1.412002	0.556	21.375	5.861	0.2124	False	False	N/A
HSCJ135710−011106	209.290027	−1.185015	ACT-CL J1357.1−0111	209.283527	−1.191765	0.396	51.516	6.963	0.1801	False	False	N/A
HSCJ135746+002431	209.441211	0.408675	ACT-CL J1357.6+0026	209.408333	0.437492	0.67	17.306	4.376	1.1047	True	False	False signal
HSCJ140707−001505	211.779312	−0.251406	ACT-CL J1407.1−0015	211.781773	−0.256624	0.57	22.5	9.649	0.1355	False	True	N/A
HSCJ140803+012048	212.011534	1.34675	ACT-CL J1407.9+0120	211.983214	1.339616	0.461	23.666	4.36	0.6137	True	False	Star
HSCJ141558+011809	213.99351	1.302471	ACT-CL J1415.9+0118	213.994344	1.305542	0.8246	20.084	4.569	0.0869	False	False	N/A
HSCJ142017+005645	215.069493	0.945796	ACT-CL J1420.2+0057	215.073566	0.95954	0.51	38.496	5.932	0.3183	False	False	N/A
HSCJ142025−004309	215.104968	−0.71928	ACT-CL J1420.4−0042	215.114975	−0.715447	0.7927	28.787	6.316	0.2887	False	False	N/A
HSCJ142032+002737	215.134538	0.460402	ACT-CL J1420.5+0027	215.138519	0.451265	0.6306	89.632	7.597	0.2453	False	True	N/A
HSCJ142103+002322	215.260753	0.389554	ACT-CL J1421.0+0022	215.262208	0.370932	0.654	49.918	5.76	0.4672	True	True	Merger
HSCJ142438+010915	216.158045	1.154275	ACT-CL J1424.6+0108	216.15	1.137449	0.622	36.917	4.129	0.4563	True	True	False signal
HSCJ142456−014152	216.234116	−1.697835	ACT-CL J1424.9−0141	216.238952	−1.686031	0.948	37.315	4.502	0.3629	True	False	None apparent
HSCJ142624−012657	216.601055	−1.449167	ACT-CL J1426.3−0126	216.594728	−1.447166	0.4528	76.091	8.103	0.138	False	False	N/A
HSCJ143607−005405	219.027581	−0.901277	ACT-CL J1436.1−0054	219.037497	−0.908114	0.69	36.61	5.065	0.308	False	True	N/A
HSCJ144031−013732	220.130763	−1.625652	ACT-CL J1440.5−0137	220.126279	−1.624222	0.3088	89.282	8.639	0.077	False	True	N/A
HSCJ144133−005358	220.38613	−0.899519	ACT-CL J1441.5−0053	220.390202	−0.890215	0.5372	49.524	4.58	0.2317	False	False	N/A
HSCJ144309+010105	220.788791	1.018041	ACT-CL J1443.1+0102	220.79119	1.041791	0.5287	31.387	6.359	0.5401	True	False	Star
HSCJ144955+005036	222.480008	0.843226	ACT-CL J1450.0+0049	222.523337	0.824991	0.382	28.364	5.259	0.8838	True	True	Star
HSCJ145219+001027	223.078667	0.174028	ACT-CL J1452.3+0009	223.07932	0.162355	0.597	40.924	6.874	0.2807	False	True	N/A
HSCJ221016+045118	332.566339	4.854976	ACT-CL J2210.1+0451	332.537481	4.854123	0.578	36.453	4.288	0.6803	True	False	Star
HSCJ221359+015127	333.497898	1.857536	ACT-CL J2213.9+0151	333.491937	1.854227	0.702	57.824	5.401	0.1755	False	True	N/A

Table A1 – *continued*

HSC name	HSC RA (°)	HSC dec (°)	ACT name	ACT RA (°)	ACT dec (°)	z	λ	SNR	r (Mpc)	Miscent.?	Merging?	Cause of miscent.
HSCJ221552+043503	333.965633	4.584258	ACT-CL J2215.8+0435	333.966651	4.589261	0.6355	85.625	5.835	0.1261	False	True	N/A
HSCJ222435+050716	336.143852	5.121022	ACT-CL J2224.5+0507	336.141515	5.12084	0.622	23.496	5.061	0.0571	False	True	N/A
HSCJ222524+044832	336.347955	4.808806	ACT-CL J2225.4+0447	336.353053	4.79926	0.5	40.588	4.858	0.2376	False	False	N/A
HSCJ222808+023325	337.033003	2.557033	ACT-CL J2228.0+0233	337.024901	2.562467	0.7835	18.588	4.968	0.2616	False	False	N/A
HSCJ222936+031840	337.398028	3.311074	ACT-CL J2229.5+0318	337.397435	3.309464	0.3006	26.702	4.67	0.0275	False	True	N/A
HSCJ223504+033326	338.766167	3.557252	ACT-CL J2235.0+0333	338.762807	3.550872	0.7381	60.172	8.556	0.1893	False	True	N/A
HSCJ225238+043142	343.15845	4.528324	ACT-CL J2252.6+0432	343.150459	4.537319	0.696	103.433	8.278	0.3084	False	True	N/A
HSCJ230235+000234	345.6461	0.042839	ACT-CL J2302.6+0002	345.651516	0.041885	0.534	75.622	6.556	0.1251	False	True	N/A
HSCJ230335+000855	345.895069	0.148492	ACT-CL J2303.5+0008	345.887408	0.141518	0.5159	61.962	4.656	0.2314	False	True	N/A
HSCJ230740+013056	346.916265	1.515519	ACT-CL J2307.6+0130	346.91726	1.515662	0.4053	73.259	10.455	0.0196	False	False	N/A
HSCJ231255−001521	348.229546	−0.255778	ACT-CL J2312.9−0013	348.22911	−0.233333	0.588	35.433	4.207	0.5352	True	False	None apparent
HSCJ231459+023150	348.746425	2.530622	ACT-CL J2314.8+0231	348.724994	2.520886	0.5812	26.991	4.417	0.5577	True	True	Star
HSCJ231833+003403	349.638652	0.567605	ACT-CL J2318.5+0033	349.629097	0.562501	0.7386	32.976	4.598	0.2845	False	True	N/A
HSCJ231950+003029	349.957945	0.508105	ACT-CL J2319.7+0030	349.948159	0.501628	0.8901	26.936	7.892	0.3281	False	True	N/A
HSCJ231953+003813	349.972636	0.637046	ACT-CL J2319.8+0038	349.968109	0.644234	0.872	30.935	5.237	0.236	False	True	N/A
HSCJ232618+003002	351.574507	0.50051	ACT-CL J2326.2+0030	351.570636	0.505178	1.1799	40.416	5.652	0.1806	False	False	N/A
HSCJ232915+005653	352.312526	0.94813	ACT-CL J2329.2+0056	352.321084	0.937561	0.742	25.08	4.663	0.3578	True	False	Merger
HSCJ233239−001350	353.163728	−0.2305	ACT-CL J2332.6−0014	353.171805	−0.247035	1.092	31.045	5.678	0.5407	True	True	Misidentified CG
HSCJ233253+011050	353.218979	1.180664	ACT-CL J2332.8+0110	353.215821	1.167041	0.48	52.484	6.939	0.3006	False	True	N/A
HSCJ233331−005630	353.378333	−0.941535	ACT-CL J2333.4−0056	353.371849	−0.943868	0.5168	25.108	4.973	0.1541	False	False	N/A
HSCJ233740+001617	354.415545	0.27138	ACT-CL J2337.6+0016	354.412551	0.272715	0.2878	88.112	23.567	0.0511	False	False	N/A
HSCJ234311+003231	355.794545	0.541862	ACT-CL J2343.1+0032	355.787502	0.541497	0.8504	40.002	6.666	0.1945	False	False	N/A
HSCJ234341+001845	355.920075	0.312438	ACT-CL J2343.7+0018	355.9282	0.306792	0.2554	104.584	7.651	0.1415	False	True	N/A
HSCJ234736+011602	356.899439	1.267264	ACT-CL J2347.6+0116	356.902542	1.268125	1.266	36.758	7.864	0.0968	False	True	N/A
HSCJ235127+004633	357.864107	0.775861	ACT-CL J2351.4+0047	357.872388	0.784359	0.436	41.036	5.146	0.2416	False	False	N/A
HSCJ235145+000916	357.936213	0.154526	ACT-CL J2351.7+0009	357.938857	0.153106	0.8588	38.777	8.349	0.083	False	False	N/A
HSCJ235628+001028	359.116487	0.174372	ACT-CL J2356.3+0009	359.097946	0.158315	1.0545	26.853	4.42	0.7156	True	True	Deblending
HSCJ235934+020824	359.889826	2.139925	ACT-CL J2359.5+0208	359.887357	2.138787	0.4303	64.955	9.27	0.0549	False	False	N/A

APPENDIX B: PROPERTIES OF MERGING VERSUS NON-MERGING CLUSTERS

Fig. B1 compares the distributions of λ and M_s between merging and non-merging clusters within the fiducial cross-match. Similar to the well-centred versus miscentred comparison in Fig. 5, the merging and non-merging distributions for both properties are inconsistent with being drawn from the same underlying distribution. Fig. B1 also suggests that merging clusters have higher λ and M_s than non-merging ones. The same effect is seen in the richness distribution for *all* HSC clusters, rather than just the sample in the fiducial cross-match. This is likely a selection effect since clusters with fewer galaxies are less likely to have multiple discernible peaks in their galaxy distribution and thus are less likely to be identified as mergers by Okabe et al. (2019).

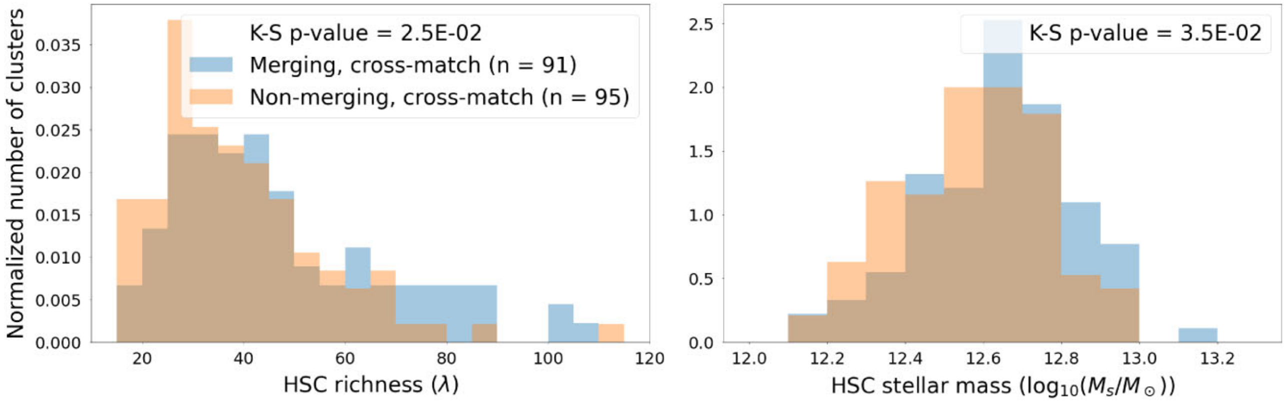

Figure B1. The normalized distributions of richness and stellar mass for both merging and non-merging clusters within the fiducial cross-match, along with the corresponding K–S test *p*-values. In this plot, merging and non-merging clusters are categorized based on the merger catalogue of Okabe et al. (2019). The *p*-values for both λ and M_s are statistically significant, indicating that merging clusters tend to have higher richnesses and stellar masses than non-merging clusters.

This paper has been typeset from a TEX/LATEX file prepared by the author.